NASA
Technical
Paper
2228

December 1983

Thrust-Induced Effects on Subsonic Longitudinal Aerodynamic Characteristics of a Vectored-Engine-Over-Wing Configuration

P. Frank Quinto and
John W. Paulson, Jr.

NASA

25th Anniversary
1958-1983

NASA
Technical
Paper
2228

1983

Thrust-Induced Effects on Subsonic Longitudinal Aerodynamic Characteristics of a Vectored-Engine-Over-Wing Configuration

P. Frank Quinto and
John W. Paulson, Jr.

Langley Research Center
Hampton, Virginia

NASA

National Aeronautics
and Space Administration

Scientific and Technical
Information Branch

1983

SUMMARY

The thrust-induced effects on the longitudinal aerodynamic characteristics of a vectored-engine-over-wing model were investigated. The investigation was conducted in the Langley 4- by 7-Meter Tunnel at Mach numbers of 0.14 to 0.17 over an angle-of-attack range from -2° to 26°. The overall thrust coefficient was varied from 0 (jet off) to 2.0. The major model variables were the spanwise-blowing nozzle sweep angle and the main nozzle vector angle along with trailing-edge flap deflections.

The results of the investigation indicate that the thrust-induced effects from the main nozzle alone were not as large as those with the spanwise nozzles and were mainly due to boundary-layer control affecting a small area aft of the nozzle. When the spanwise nozzles were included, the induced effects were larger (more so for the spanwise blowing sweep angle of 40° than for 60°) and were due to both boundary-layer control and induced circulation lift. The leading-edge vortex effect was generally not evident for either spanwise blowing sweep angle.

INTRODUCTION

In the operation of the next generation of fighter aircraft, one of the major areas of emphasis is the short take-off and landing (STOL) performance. The STOL performance is needed so that fighter aircraft can operate from bomb-damaged runways (usable runway length of about 1500 ft). To meet this STOL requirement, the use of improved high-lift systems and thrust effects will be needed. These thrust effects are divided into two categories: direct effects and induced effects. The direct effects consist of deflecting (or vectoring) the thrust in the lift direction. The induced effects are brought about by the presence of the jet exhaust inducing flows that would not be present without the jet and include boundary-layer control (BLC), induced circulation, and leading-edge vortices.

The vectored-engine-over-wing (VEO-wing) configuration uses both direct and induced thrust effects to achieve its STOL performance. (See ref. 1.) The VEO-wing configuration (as described in refs. 2 to 7) uses engines mounted over the wing to blow exhaust gases over the trailing-edge flap (similar to upper-surface-blowing transports) and part of the exhaust is diverted for spanwise blowing over the wing upper surface. These propulsion methods are intended to produce increases in lift through additional induced circulation by a jet-flap effect and through leading-edge vortex flows produced by spanwise blowing for better low-speed (STOL) operations. (See refs. 8 to 12.)

Several low-speed tests have been conducted on the VEO-wing fighter-configuration model. (See refs. 2 to 7.) However, in these tests, the thrust-induced effects were not fully addressed. This last test was conducted in the Langley 4- by 7-Meter Tunnel to investigate these thrust-induced effects in detail. The configuration was tested at Mach numbers ranging from 0.14 to 0.17 and over an angle-of-attack range from -2° to 26°. The wing trailing edge was deflected from 0° to 30°. The overall thrust coefficients, spanwise-blowing nozzle and main nozzle combined, were varied from 0 (jet off) to 2.0.

MODEL DESCRIPTION

The model used in this investigation was a 0.108-scale powered-lift model of a fighter-type canard-wing configuration with podded nacelles over the wing, as shown in figures 1 and 2. The model geometric characteristics are given in table I. The leading-edge sweep of the wing was 40° and of the canard was 55°. The wing had an inboard and an outboard trailing-edge flap. The inboard trailing-edge flap was located behind the engine nozzle. The inlet of the nacelle was faired over; inlet flow could not be simulated since the interior volume of the nacelle was needed to house the propulsion simulation system.

The model was supported by an air sting through which high-pressure air was supplied from an external source. The air line through the sting was designed to minimize any transfer of mechanical forces from the air supply to the model balance. The high-pressure air passed from the air line to the model plenum and through each nacelle, where separate control valves were used to balance the flow between the left and right nozzles. Each nacelle had a pair of nozzles, a chordwise main nozzle and a spanwise-blowing nozzle as shown in figure 3. The main nozzles were two-dimensional convergent-divergent half wedge nozzles. The half-wedge, or lower ramp, surface was used to help turn the exhaust flow over the trailing-edge flap system. (See figs. 3 and 4.) The ramp was interchangeable to allow increased nozzle turning angles when high flap deflections were used and to maintain constant total nozzle area (main and spanwise) when the spanwise nozzles were used. The spanwise-blowing nozzles were louvered flush nozzles which allowed for two spanwise-blowing nozzle sweep angles of 40° and 60°, as shown in figure 5. The following six configurations were tested in this investigation. (A list of symbols and abbreviations used in this paper appears after the references):

Configuration	δ_f, deg	Nozzles
1	0	Main
2	15	Main
3	30	Main
4	0	Main and spanwise (Λ_s = 40°)
5	30	Main and spanwise (Λ_s = 40°)
6	30	Main and spanwise (Λ_s = 60°)

MODEL INSTRUMENTATION

Since the intent of this investigation was to examine thrust-induced effects rather than nozzle performance, only minimal nozzle pressure instrumentation was used. These pressures were used to determine nozzle total pressure for calculating nozzle thrust levels. To determine the mass-flow rate of the high-pressure air to the model, a venturi flowmeter was mounted at the air supply station, outside the test section. The forces and moments were measured with a six-component strain-gage balance mounted internal to the model. The angle of attack of the model was measured with an accelerometer also mounted internal to the model.

FLOW VISUALIZATION

To observe the thrust effects created by the main and spanwise nozzles, fluorescent minitufts were installed on the left half of the VEO-wing model, as shown in figure 6. The minitufts were very thin monofilament nylon with diameters of 0.0019 in. and 0.0038 in. The larger filament was used near the exits of the main and spanwise nozzles, where high-pressure, high-velocity air tended to destroy the smaller filaments. The left side of the model was painted black to reduce the reflection and glare created by the high-intensity strobe lamps. An ultraviolet-transmission glass filter was installed over each of the four high-intensity strobe lamps in order to fluoresce the minitufts. The minitufts were attached to the model surface with cyanoacrylate adhesive, as detailed in reference 13. Photographs of the minitufts were obtained with a 70-mm camera with high-speed film (ASA 400).

STATIC CALIBRATION AND DATA REDUCTION

Since these nozzles had been calibrated extensively in prior tests (see refs. 2 to 7), a very limited static calibration was performed on each nozzle configuration before this investigation. This calibration was made to verify that the nozzle performance was the same as that obtained in the previous calibrations.

The static characteristics of the nozzle thrust force T, gross thrust coefficient C_T, and jet deflection angle θ_j were determined for each configuration as follows:

$$T = \sqrt{F_N^2 + F_A^2} \tag{1}$$

$$C_T = T_p p_\infty / qS \tag{2}$$

$$\theta_j = -\tan^{-1}(F_N/F_A) \tag{3}$$

Also, the total nozzle pressure ratio NPR was determined by using the following equation:

$$NPR = (p_{t,t}/p_\infty)[A_t/(A_s + A_t)] + (p_{t,s}/p_\infty)[A_s/(A_s + A_t)] \tag{4}$$

The main nozzle total pressure $p_{t,t}$ was measured with total-pressure probes just upstream of the nozzle throat, and the spanwise nozzle total pressure $p_{t,s}$ was obtained by using the static test results of reference 7 and the main nozzle total pressure of this test. Sample plots of these results are presented in figure 7(a) for the main nozzle alone (no spanwise blowing) with a flap deflection of 15° and in figure 7(b) for the main and spanwise nozzles with a flap deflection of 30°.

For the wind-on test, the data were corrected for base pressure, air line and balance interaction, and pressurized air sting. To examine the thrust-induced effects on the VEO-wing configuration, the gross thrust coefficient from the static investigation was related to wind-on conditions by equation (2) because no separate measurement of the thrust could be obtained during wind tunnel runs. The balance in the model measured total forces and moments (aerodynamic and propulsion). The direct thrust components were removed from the aerodynamic data as follows:

$$C_{L,TR} = C_L - C_T \sin(\alpha + \theta_j) \quad (5)$$

$$C_{D,TR} = C_D + C_T \cos(\alpha + \theta_j) \quad (6)$$

$$C_{m,TR} = C_m + (x/\bar{c})C_T \sin \theta_j + (z/\bar{c})C_T \cos \theta_j \quad (7)$$

TEST CONDITIONS

This investigation was performed in the Langley 4- by 7-Meter Tunnel over an angle-of-attack range from -2° to 26° without sideslip or roll angles. Data were obtained at dynamic pressures q of 30 lbf/ft^2 and 40 lbf/ft^2, and the thrust was varied to give a C_T range from 0 (jet off) to 2.0 as follows:

C_T	q, lbf/ft^2	T, lbf
0	40	0
.1	↓	14.0
.2		28.0
.3		42.0
.4		56.0
.5		70.0
.75		105.0
.9		126.0
1.5		210.0
2.0	30	210.0

At $q = 40$ lbf/ft^2, the Reynolds number per foot, based on $\bar{c}$, was 1.17×10^6, and the corresponding Mach number was 0.17; at $q = 30$ lbf/ft^2, the Reynolds number was 1.04×10^6, and the Mach number was 0.14.

PRESENTATION OF RESULTS

The results of this investigation are presented in the following figures:

DISCUSSION

Total Longitudinal Aerodynamic Characteristics

The total longitudinal aerodynamic characteristics for the six VEO-wing configurations are presented in figures 8 to 13. Included in the total longitudinal data are the direct jet effects and the thrust-induced effects. Figures 8 to 10 present the results for the main nozzle alone exhausting over different trailing-edge flap deflections. The results indicate the expected increases in lift and nose-down pitching moment as either thrust coefficient or flap deflection increases. In addition, as C_T increases, the drag polar shifts towards the negative drag coefficient, or thrust direction, in proportion to the thrust coefficient.

The results for the main and 40°-sweep spanwise-blowing nozzles are presented in figure 11 for an undeflected trailing edge and in figure 12 for a 30° trailing-edge flap deflection. Figure 13 presents the results of the main and 60°-sweep spanwise-blowing nozzles with a 30° trailing-edge flap deflection. The results for the three spanwise-blowing nozzle configurations indicate increases in lift and nose-down pitching moment and shifts toward negative drag coefficients in the drag polar as

C_T increases. The three spanwise configurations resulted in little change in nose-down pitching moment, but resulted in greater increases in lift and greater improvement of the drag polars than the main-nozzle-alone configuration. The increases and improvements are due to the spanwise-blowing nozzle affecting more of the wing than the main nozzle alone, and this is further discussed subsequently.

Thrust-Removed Longitudinal Aerodynamic Characteristics

Figures 14 to 19 are the data from figures 8 to 13 with the direct thrust component removed. The results of the main-nozzle-alone configurations are presented in figures 14 to 16. For all three configurations (δ_f = 0°, 15°, and 30°), the lift increases throughout the angle-of-attack range and lift-drag polars improve above $\alpha \approx 10°$ as thrust coefficient increases. The increase in the lift is due to the thrust-induced effects, which are discussed subsequently. The pitching-moment curve does not change significantly as thrust coefficient increases.

The thrust-removed results for main and 40°-sweep spanwise-blowing nozzles with δ_f = 0° and 30° are presented in figures 17 and 18, and results for main and 60°-sweep spanwise-blowing nozzles with δ_f = 30° are presented in figure 19. The results indicate larger lift increases and lift-drag polar improvements than for the main-nozzle-alone configuration as C_T increases. This may be because of the spanwise jet affecting the wing in several ways: (1) a cambering of the wing upper surface, in which the free stream flows over the spanwise jet rather than the actual wing surface; (2) a jet-flap effect, which occurs when the free stream turns the spanwise jet which then flows over the trailing-edge flaps, creating additional circulation; (3) the spanwise jet reattaching some of the separated flow on the wing and flap; and (4) the leading-edge vortex caused by the spanwise jet. When a concentrated spanwise jet, near and parallel to the wing leading edge, is introduced on a moderately swept wing at incidence, a leading-edge vortex is generated and stabilized as indicated in references 8 and 9. Associated with the leading-edge vortex is a nonlinear increase in lift above attached or potential flow conditions (ref. 10). This nonlinear lift increase is apparent only for the 40°-sweep spanwise-blowing nozzle (figs. 17 and 18) at C_T = 2.0. At all other conditions this vortex lift is not clearly evident, indicating little or no leading-edge vortex effects. A probable reason for the absence of these effects is that a discrete, concentrated jet flow (as investigated in refs. 8 and 9) is not produced by the spanwise nozzles of this investigation. Although the nonlinear increase is not present at each C_T, the spanwise jet does increase lift and improve the drag polar as C_T increases.

The flow visualization photographs of minitufts (see figs. 30 and 31 for main and 40°-sweep spanwise-blowing nozzles and fig. 32 for main and 60°-sweep spanwise-blowing nozzles) indicate little change in the vicinity of the wing leading edge to indicate a vortex flow as C_T increases from jet off (C_T = 0) to jet on (C_T > 0). If a leading-edge vortex is present because of the spanwise jet, the tufts around the wing leading edge are aligned in a spanwise direction but not parallel to one another. Further aft of this area (behind the vortex), the tufts are aligned in a chordwise direction and approximately parallel to one another, indicating an attached flow condition aft of the leading-edge vortex. In both spanwise-blowing nozzle configurations (Λ_s = 40° and 60°), the photographs do not show such flows occurring on the wing as C_T increases.

Thrust-Induced Longitudinal Aerodynamic Characteristics

Evaluation of thrust-induced longitudinal aerodynamic characteristics was performed in a manner similar to that in references 11, 12, 14, and 15, in which the different components of powered lift were isolated from the total coefficient (thrust included) and presented as a function of C_T. A typical component breakdown is shown in figure 20. As can be seen, the total lift coefficient can be broken down into

1. Basic configuration lift - the lift of the model with undeflected flaps and jet off

2. Flap lift - the lift due to a flap deflection with jet off

3. Jet reaction lift - the thrust component in the lift direction when the jet is deflected or vectored

4. Thrust-induced lift - the lift due to additional circulation from a jet-flap effect, reattachment of separated flow (BLC), and leading-edge vortex from spanwise blowing

The thrust-induced lift increment $\Delta C_{L,\Gamma}$ can be further broken down into boundary-layer control (BLC) and induced circulation lift, as shown in figure 21 and as found in references 11, 12, and 14 to 17. As noted, the demarcation between BLC and circulation lift can be defined as the point on the induced lift curve at which the slope changes from steep to moderate (the "knee" of the curve). A similar breakdown is possible for the components of drag and pitching moment.

The equations defining the thrust-induced coefficient increments are presented below, in which the jet-off configuration aerodynamic characteristics and the direct thrust component are removed from the jet-on aerodynamic characteristics:

$$\Delta C_{L,\Gamma} = C_{L,TR} - C_L\Big|_{C_T=0} \tag{8}$$

$$\Delta C_{D,\Gamma} = C_{D,TR} - C_D\Big|_{C_T=0} \tag{9}$$

$$\Delta C_{m,\Gamma} = C_{m,TR} - C_m\Big|_{C_T=0} \tag{10}$$

Main nozzle alone.- The thrust-induced longitudinal aerodynamic increments of the three main-nozzle-alone configurations are presented in figures 22 to 24. In these three configurations (δ_f = 0°, 15°, and 30°), the thrust-induced lift coefficient increment $\Delta C_{L,\Gamma}$ levels are not large compared with those for the combined main and spanwise-blowing nozzle configurations. (See figs. 25 to 27.) At $C_T \approx 1.0$, $\Delta C_{L,\Gamma} < 0.3$ for $\alpha = 16°$. The general shape of the $\Delta C_{L,\Gamma}$ curves is similar to the example of figure 21, and the curves show primarily BLC rather than induced circulation lift. It is interesting that at the smallest trailing-edge deflection ($\delta_f = 0°$), the $\Delta C_{L,\Gamma}$ curves indicate more circulation lift than when the flap is deflected. This is attributed to a viscous entrainment effect, which is apparently reduced as trailing-edge deflection increases. The induced lift increments (when $\delta_f = 0°$) become larger as angle of attack is increased, which may be because of increased flow separation on the wing which can be reattached by the main nozzle entrainment effect. Since this entrainment effect is reduced as trailing-edge deflection increases, the effect of increasing angle of attack is reduced.

In figures 22 to 23, the pitching-moment and drag coefficient increments for the three configurations show similar trends as those reported in references 15 and 16. The thrust-induced pitching-moment coefficient increments indicate a nose-down increment because of relatively aft loading on the wing. The thrust-induced drag coefficient increments are approximately equal to the increment in thrust-induced drag expected for an increase in C_L. At low thrust coefficients, the values of $\Delta C_{D,\Gamma}$ are negative because the flow on the wing behind the main nozzle is separated and the base area behind the nozzle has a low pressure at $C_T = 0$. At $C_T > 0$ (jet on), the flow on the wing is reattached and the base area is occupied by the main nozzle exhaust, causing a decrease in $\Delta C_{D,\Gamma}$. The flow separation and reattachment is shown in figure 28 by the change in tuft position aft of the main nozzle as thrust is increased from jet off to jet on.

As a measure of the magnitude of the thrust-induced effects on the VEO-wing configuration, the following method is used. First, typical values of approach glide slope angle and angle of attack for STOL operations are chosen. Next, the total aerodynamic lift-drag polar and thrust-induced lift curves are used to determine the landing thrust coefficient and $\Delta C_{L,\Gamma}$. Typical values of glide slope angle and angle of attack for STOL operations are -6° and 16° for this configuration. The glide slope angle is defined as

$$\gamma = -\tan^{-1}(C_D/C_L) \tag{11}$$

With the values of angle of attack, glide slope angle, and C_D/C_L, the thrust coefficient can be determined from the total lift-drag polars. Once the C_T is known, the thrust-induced lift increment can be determined from the plots in figures 22 to 27. From this analysis, the thrust coefficient for the main-nozzle-alone configuration with $\delta_f = 30°$ is about 0.4 and the corresponding $\Delta C_{L,\Gamma}$ is 0.25 (fig. 24), which is about 11 percent of the total lift coefficient of 2.25.

Main and spanwise-blowing nozzles.- The thrust-induced longitudinal increments for the three spanwise-blowing configurations are presented in figures 25 to 27. The general shape of the thrust-induced lift increment indicates contribution from both BLC and circulation lift. The values of $\Delta C_{L,\Gamma}$ for main and spanwise-blowing nozzle configurations are higher than for the main-nozzle-alone configurations because the spanwise jet affects a larger portion of the wing. As in the main-nozzle-alone configuration, the effect of increasing angle of attack is decreased when $\delta_f > 0°$ because of the reduced entrainment effects. The two different spanwise-blowing nozzle sweep angles had different effects on the wing. The 40°-sweep spanwise-blowing nozzle affected a larger portion of the wing, whereas the 60°-sweep nozzle only affected portions of the inboard wing and the trailing-edge flaps. The effect of the spanwise-blowing nozzles is shown in the flow visualization photographs in figures 30 to 32. Figures 30 and 31 show the area affected by the 40°-sweep spanwise jet. The affected area is shown by the minituft remnants, since the minitufts fatigued because of the high-speed spanwise jet flow. In figure 32, the area affected by the 60°-sweep spanwise jet can be shown by the minitufts on the outboard trailing-edge flap (near the main nozzle). At $C_T = 0$, the minitufts indicate a spanwise flow; when $C_T > 0$, the minitufts indicate a relatively chordwise flow. The affected area is much less than for the 40°-sweep spanwise jet. Also in figures 30 to 32, the area behind the nozzle shows separated flow at $C_T = 0$; the flow reattaches at $C_T > 0$, as previously mentioned for the main-nozzle-alone configurations. In the flow visualization photographs of the main and spanwise-blowing nozzle configurations, two separate blowing effects are present, one mainly due to the main nozzle and the other totally due to the spanwise-blowing nozzle. The effects are summarized in figure 33. They are also present in the thrust-induced-increment data. In figures 25 and 26, the general trend exhibits "double knees"; one knee is due to the main nozzle jet attaching the inboard trailing-edge flap and the spanwise jet not penetrating the flow enough to affect the wing at low thrust coefficients, and the second knee is totally due to the spanwise nozzle affecting the outboard wing at higher thrust coefficients. This double knee is more apparent with $\delta_f = 30°$ than with $\delta_f = 0°$, because of the entrainment effect at $\delta_f = 0°$.

To determine the effect of the main and spanwise-blowing nozzles on the landing configuration lift, the same method previously discussed for the main-nozzle-alone configuration is used. For the main and 40°-sweep spanwise-blowing nozzles with $\delta_f = 30°$, the C_T is about 0.5, which corresponds to a thrust-induced lift increment of 0.47; this is 18.5 percent of the total lift coefficient of 2.54. The thrust-induced increment for the main and 60°-sweep spanwise-blowing nozzles with $\delta_f = 30°$ has a smaller value of 0.33 at $C_T \approx 0.5$, which is 13.6 percent of $C_L = 2.45$. The C_T for the landing configuration for all three VEO-wing configurations at $\delta_f = 30°$ is about 0.5.

CONCLUSIONS

An investigation of the thrust-induced effects on the longitudinal aerodynamic characteristics of the vectored-engine-over-wing (VEO-wing) configuration was conducted in the Langley 4- by 7-Meter Tunnel. The VEO-wing was tested at Mach numbers ranging from 0.14 to 0.17 over an angle-of-attack range from -2° to 26°. The wing trailing edge was deflected from 0° to 30°. The overall thrust coefficients, main and spanwise-blowing nozzles combined, were varied from 0 to 2.0. The results of this investigation indicate the following:

1. With the main nozzle alone, the majority of the thrust-induced effects were the result of boundary-layer control more than induced circulation lift; the only area affected was near the rear of the nozzle, except for the undeflected trailing-edge flap configuration.

2. In both 40°- and 60°-sweep spanwise-blowing nozzle configurations, the leading-edge vortex effects were generally not evident, but the spanwise jet did increase the lift and improve the drag polar as thrust coefficient increased.

3. The effect of increasing angle of attack on induced lift decreased when the trailing edge was deflected because of the reduced entrainment effects in both the main-nozzle-alone and the main and spanwise-blowing nozzle configurations.

4. In the main and spanwise-blowing nozzle configurations, the thrust-induced lift increments were obtained from two effects. The first was from the main nozzle jet attaching the flow over the inboard flap, and the second was from the spanwise nozzle jet affecting the outboard portion of the wing.

5. The thrust-induced increments were larger for the spanwise-blowing angle of 40° than for the 60° angle, since the 40°-sweep spanwise nozzle jet affected more of the wing. Both spanwise configurations exhibited boundary-layer control and induced circulation lift.

6. The VEO-wing landing configuration with the highest value of thrust-induced lift increment was the main and 40°-sweep spanwise-blowing nozzles with 30° trailing-edge flap deflection. The thrust-induced lift increment value of this configuration was 18.5 percent of the total lift coefficient of 2.54.

Langley Research Center
National Aeronautics and Space Administration
Hampton, VA 23665
November 8, 1983

REFERENCES

1. Whitten, P. D.; and Howell, G. A.: Investigations of the VEO-Wing Concept in an Air-to-Ground Role. AFFDL-TR-79-3031, U.S. Air Force, Mar. 1979.

2. Whitten, P. D.: An Experimental Investigation of a Vectored-Engine-Over-Wing Powered-Lift Concept, Volume II - High Angle of Attack and STOL Tests. AFFDL-TR-76-92, Volume II, U.S. Air Force, Mar. 1978.

3. Huffman, Jarrett K.; and Fox, Charles H., Jr.: Subsonic Longitudinal Aerodynamic Characteristics of a Vectored-Engine-Over-Wing Configuration Having Spanwise Leading Edge Vortex Enhancement. NASA TM X-73955, 1977.

4. Leavitt, Laurence D.; and Yip, Long P.: Effects of Spanwise Nozzle Geometry and Location on the Longitudinal Aerodynamic Characteristics of a Vectored-Engine-Over-Wing Configuration at Subsonic Speeds. NASA TP-1215, 1978.

5. Leavitt, Laurence D.: Longitudinal Aerodynamic Characteristics of a Vectored-Engine-Over-Wing Configuration at Subsonic Speeds. NASA TP-1533, 1979.

6. Howell, George A.: Low-Speed Wind Tunnel Investigation of the Vectored-Engine-Over-Wing Concept With Podded Nacelles. AFWAL-TR-82-3009, U.S. Air Force, Mar. 1982.

7. Paulson, John W.; Whitten, Perry D.; and Stumpfl, Stephen C.: Wind-Tunnel Investigation of the Powered Low-Speed Longitudinal Aerodynamics of the Vectored-Engine-Over (VEO) Wing Fighter Configuration. NASA TM-83263, 1982.

8. Campbell, James F.: Effects of Spanwise Blowing on the Pressure Field and Vortex-Lift Characteristics of a 44° Swept Trapezoidal Wing. NASA TN D-7907, 1975.

9. Erickson, Gary E.; and Campbell, James F.: Improvement of Maneuver Aerodynamics by Spanwise Blowing. NASA TP-1065, 1977.

10. Polhamus, Edward C.: Predictions of Vortex-Lift Characteristics by a Leading-Edge Suction Analogy. J. Aircr., vol. 8, no. 4, Apr. 1971, pp. 193-199.

11. Campbell, John P.: Overview of Powered-Lift Technology. Powered-Lift Aerodynamics and Acoustics, NASA SP-406, 1976, pp. 1-27.

12. Mavriplis, Fotis; and Gilmore, David: Investigation of Externally Blown Flap Airfoils With Leading Edge Devices and Slotted Flaps. V/STOL Aerodynamics, AGARD-CP-143, Oct. 1974, pp. 7-1 - 7-12.

13. Crowder, J. P.: Fluorescent Mini-Tufts for Non-Intrusive Flow Visualization. MDC J7374, McDonnell Douglas Corp., Feb. 1, 1977.

14. Paulson, J. W., Jr.: An Analysis of Thrust-Induced Effects on the Longitudinal Aerodynamics of STOL Fighter Configurations. AIAA-80-1879, Aug. 1980.

15. Paulson, John W., Jr.: Thrust-Induced Aerodynamics of STOL Fighter Configurations. Tactical Aircraft Research and Technology, Volume I, NASA CP-2162, Part 2, 1981, pp. 695-712.

16. Paulson, John W., Jr.; and Thomas, James L.: Summary of Low-Speed Longitudinal Aerodynamics of Two Powered Close-Coupled Wing-Canard Fighter Configurations. NASA TP-1535, 1979.

17. Banks, Daniel W.; Quinto, P. Frank; and Paulson, John W., Jr.: Thrust-Induced Effects on Low-Speed Aerodynamics of Fighter Aircraft. NASA TM-83277, 1982.

SYMBOLS

All data are reduced to coefficient form and are presented in the stability axis system. The units in this report are the U.S. Customary Units. Also, the measurements and calculations were made in U.S. Customary Units. The model moment center was located at 25 percent of the wing mean aerodynamic chord.

A_e main nozzle exit area, in^2

A_s spanwise nozzle throat area, in^2

A_t main nozzle throat area, in^2

C_D drag coefficient, Drag/qS

$C_{D,TR}$ thrust-removed drag coefficient, $C_D + C_T \cos(\alpha + \theta_j)$

$\Delta C_{D,\Gamma}$ thrust-induced drag coefficient increment, $C_{D,TR} - C_D|_{C_T=0}$

C_L lift coefficient, Lift/qS

$C_{L,TR}$ thrust-removed lift coefficient, $C_L - C_T \sin(\alpha + \theta_j)$

$\Delta C_{L,\Gamma}$ thrust-induced lift coefficient increment, $C_{L,TR} - C_L|_{C_T=0}$

C_m pitching-moment coefficient, Pitching moment/$qS\bar{c}$

$C_{m,TR}$ thrust-removed pitching-moment coefficient,
$C_m + (x/\bar{c})C_T \sin \theta_j + (z/\bar{c})C_T \cos \theta_j$

$\Delta C_{m,\Gamma}$ thrust-induced pitching-moment coefficient increment, $C_{m,TR} - C_m|_{C_T=0}$

C_T gross thrust coefficient, $T_p p_\infty/qS$

$\bar{c}$ mean aerodynamic chord, 12.303 in.

F_A axial force, lbf

F_N normal force, lbf

h_e main nozzle exit height, in. (fig. 4)

h_t main nozzle throat height, in. (fig. 4)

NPR area-weighted overall nozzle pressure ratio,
$NPR = (p_{t,t}/p_\infty)[A_t/(A_s + A_t)] + (p_{t,s}/p_\infty)[A_s/(A_s + A_t)]$

$p_{t,t}$ main nozzle total pressure, lbf/ft^2

$p_{t,s}$ spanwise nozzle total pressure, lbf/ft^2

p_∞ tunnel static pressure, lbf/ft^2

q dynamic pressure, lbf/ft^2

S	wing reference area, 3.5 ft^2
T	static thrust force, $\sqrt{F_N^2 + F_A^2}$, lbf
T_p	static thrust divided by static pressure, T/p_∞
x	longitudinal distance from thrust vector to moment reference, in.
z	vertical distance from thrust vector to moment reference, in.
α	angle of attack, deg
γ	glide slope angle, $-\tan^{-1}(C_D/C_L)$, deg
δ_f	wing trailing-edge deflection (both inboard and outboard flap and positive trailing-edge down), deg
θ_j	jet deflection angle, $-\tan^{-1}(F_N/F_A)$, deg
θ_R	nozzle ramp angle, deg
Λ_s	spanwise-blowing angle, deg

Abbreviations:

BL	butt line, in.
BLC	boundary-layer control
FS	fuselage station, in.
WCP	wing chord plane, WL = -1.388 in.
WL	water line, in.

TABLE I. - GENERAL MODEL GEOMETRIC CHARACTERISTICS

Wing:	
Wing area, ft^2	3.5
Aspect ratio	3.75
Wing span, in.	43.474
Leading-edge sweepback, deg	40
Taper ratio	0.4
Root chord, in.	16.565
Tip chord, in.	6.625
Mean aerodynamic chord, in.	12.303
Longitudinal leading-edge location (fuselage station), in.	44.547
Lateral location, in.	9.315
Canard:	
Panel area, ft^2	704
Aspect ratio	2.1
Semispan, in.	7.30
Leading-edge sweep, deg	55
Trailing-edge sweep, deg	18.28
Taper ratio	0.268
Root chord, in.	10.952
Tip chord, in.	2.939
Mean aerodynamic chord, in.	7.716
Location of quarter-chord:	
BL, in.	9.95
FS, in.	37.79
Airfoil section, percent	4 (biconvex)
Body:	
Length, in.	70.00
Maximum cross-sectional area (6.25-in. diam), in^2	30.68
Fineness ratio	11.20
Nacelle:	
Length, in.	25.4
Width, in.	3.9
Height, in.	3.2

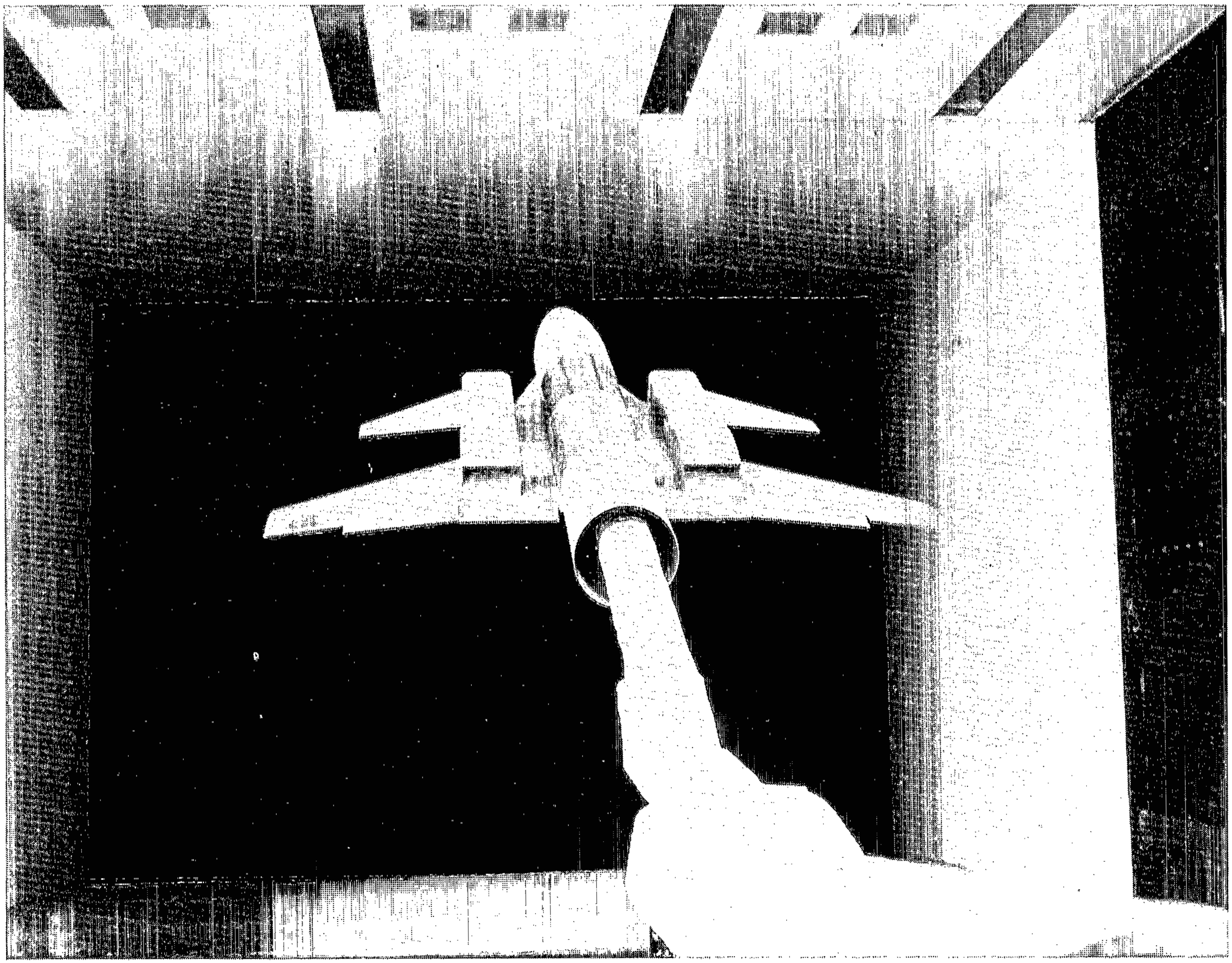

L-79-1830

Figure 1.- Rear view of vectored-engine-over-wing model installed in the Langley 4- by 7-Meter Tunnel.

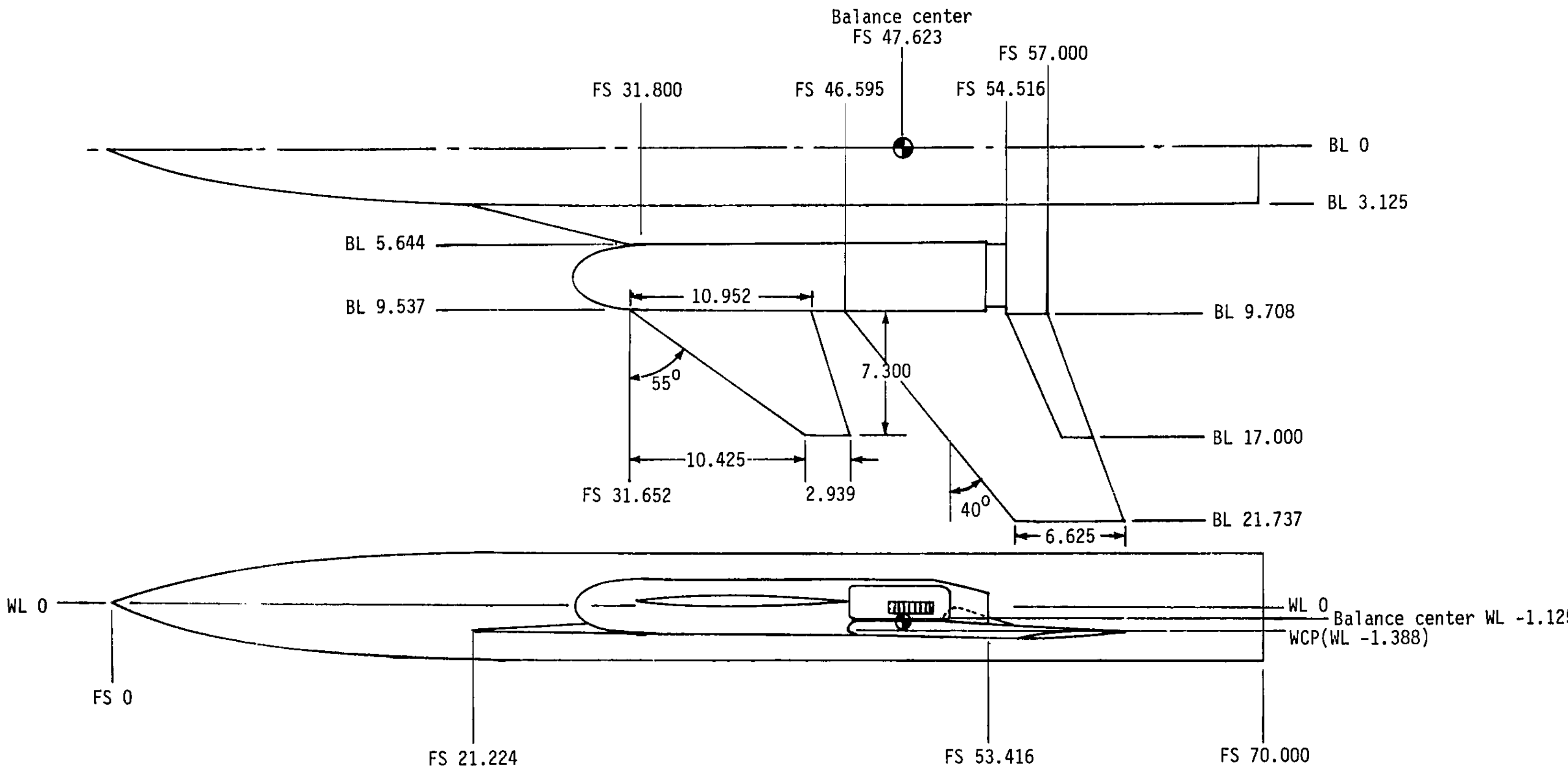

Figure 2.- Sketch of vectored-engine-over-wing model. Dimensions are in inches unless otherwise noted.

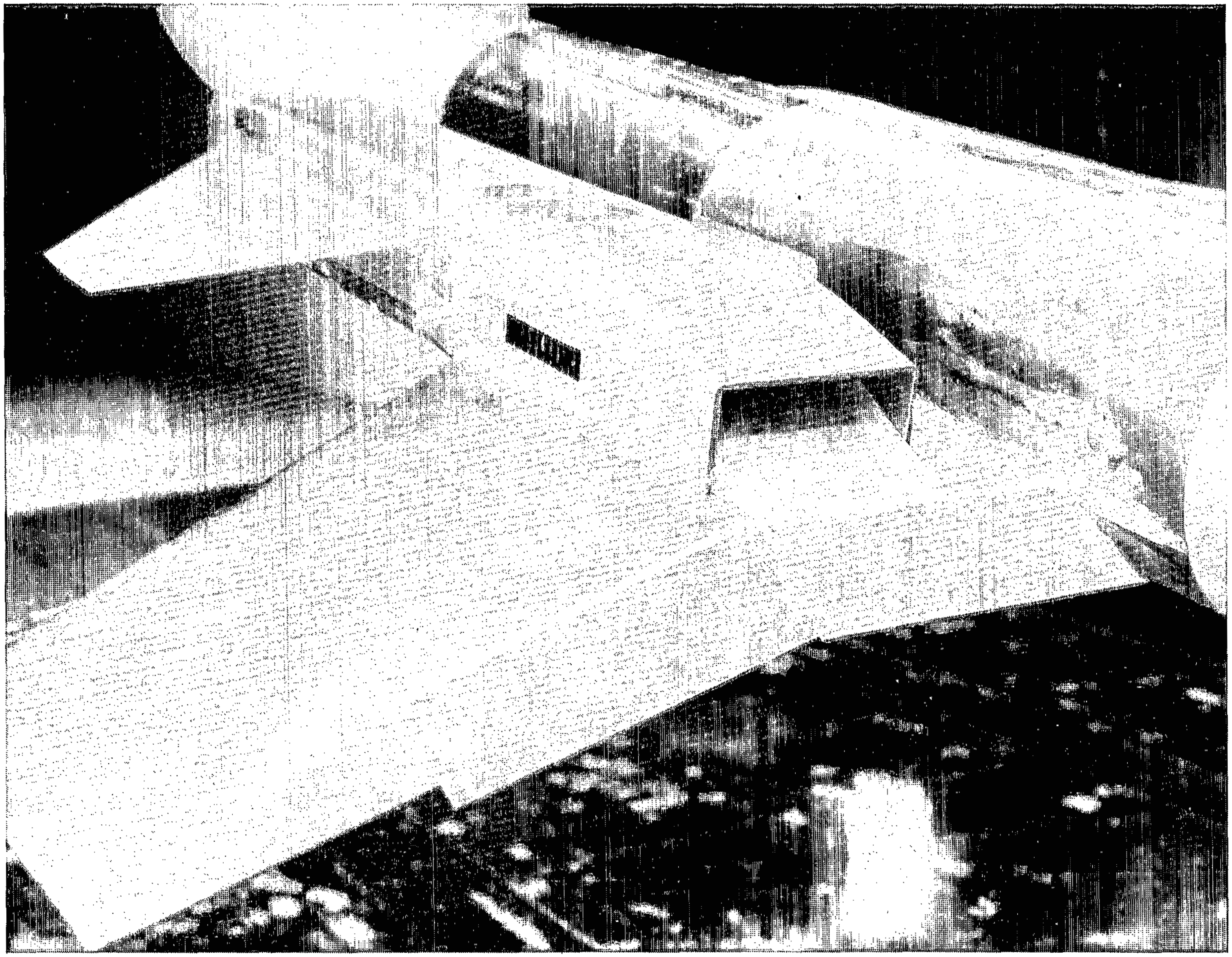

L-79-1833

Figure 3.- Three-quarter rear view of the chordwise main nozzle and spanwise-blowing nozzle of the VEO-wing model.

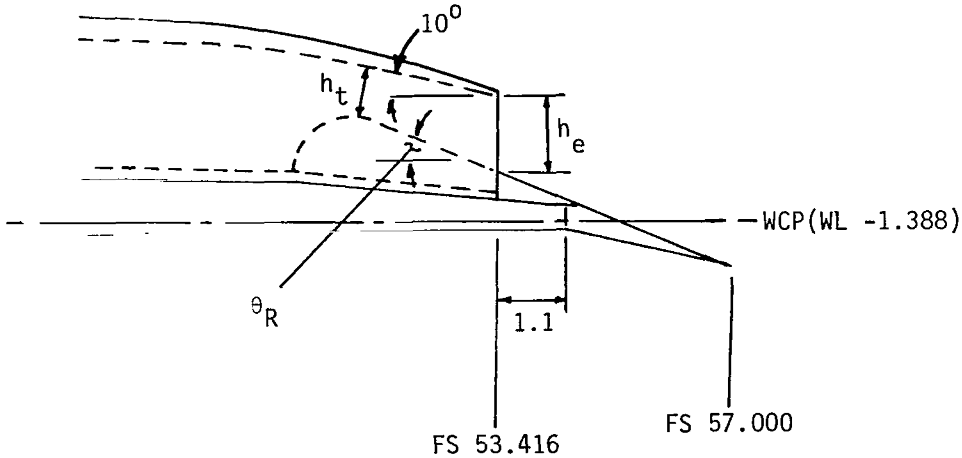

Ramp	A_t, in^2/side	A_e, in^2/side	h_t, in.	h_e, in.	θ_R, deg	Remarks
1	3.585	4.828	0.94	1.27	20	Main nozzle alone
2	3.585	4.257	.94	1.12	25	Main nozzle alone
3	2.603	3.772	.68	.99	25	Main and spanwise-blowing nozzles

Figure 4.- Nozzle geometries of the VEO-wing model. Dimensions are in inches unless otherwise noted.

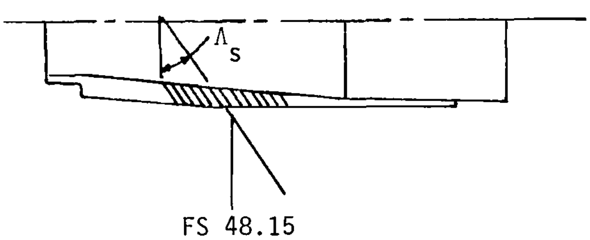

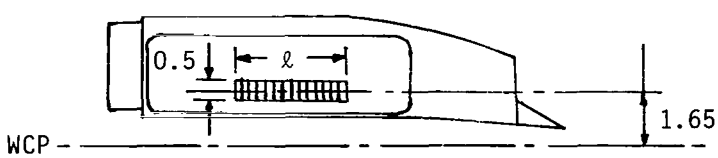

Λ_s, deg	ℓ, in.	A_s, in^2/side
40	2.15	1.000
60	4.16	1.040

Figure 5.- Spanwise nozzle geometries of the VEO-wing. Dimensions are in inches unless otherwise noted.

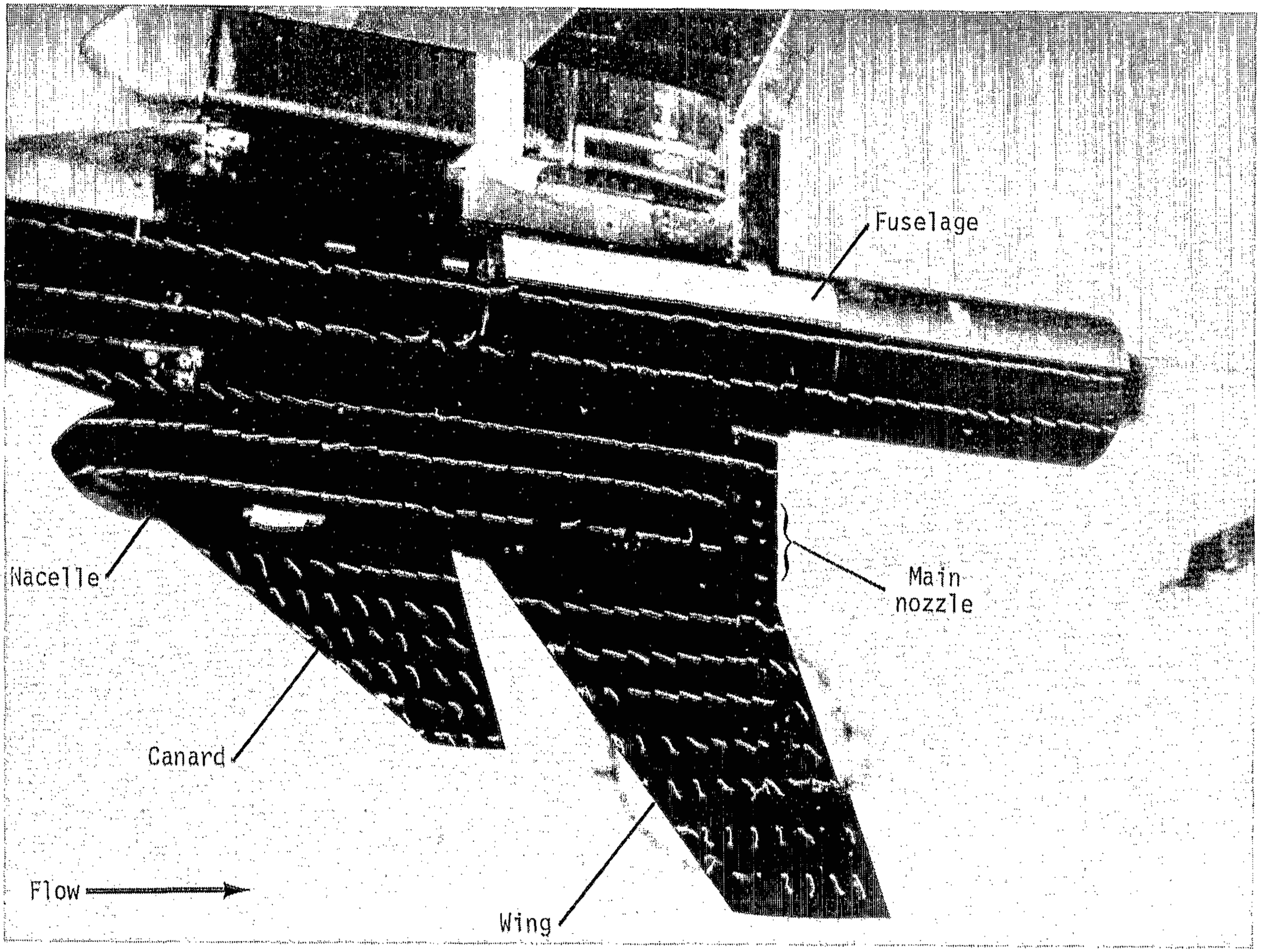

L-83-116

Figure 6.- Minituft location on VEO-wing model.

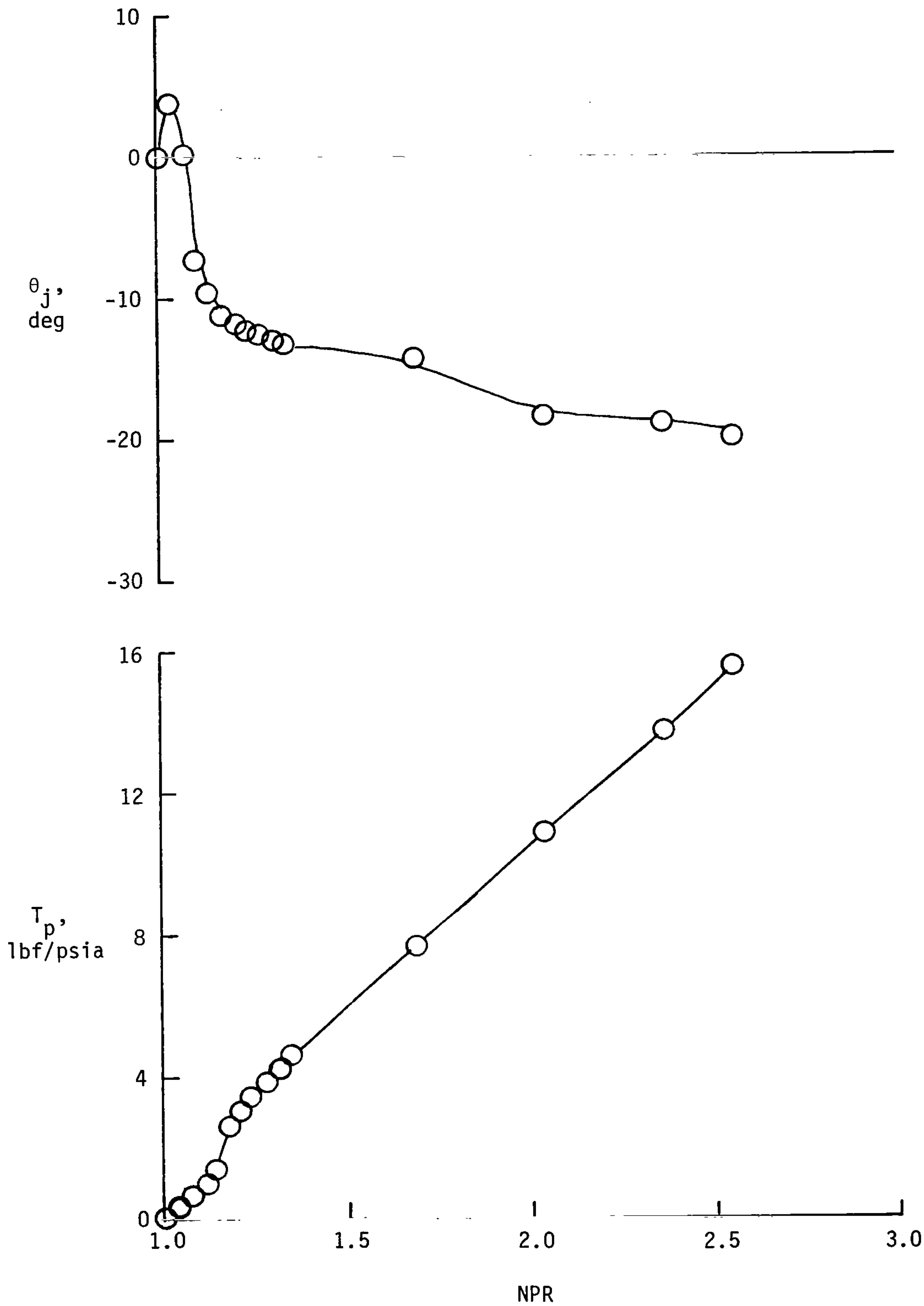

(a) Main nozzle alone; δ_f = 15°.

Figure 7.- Thrust characteristics as a function of nozzle pressure ratio.

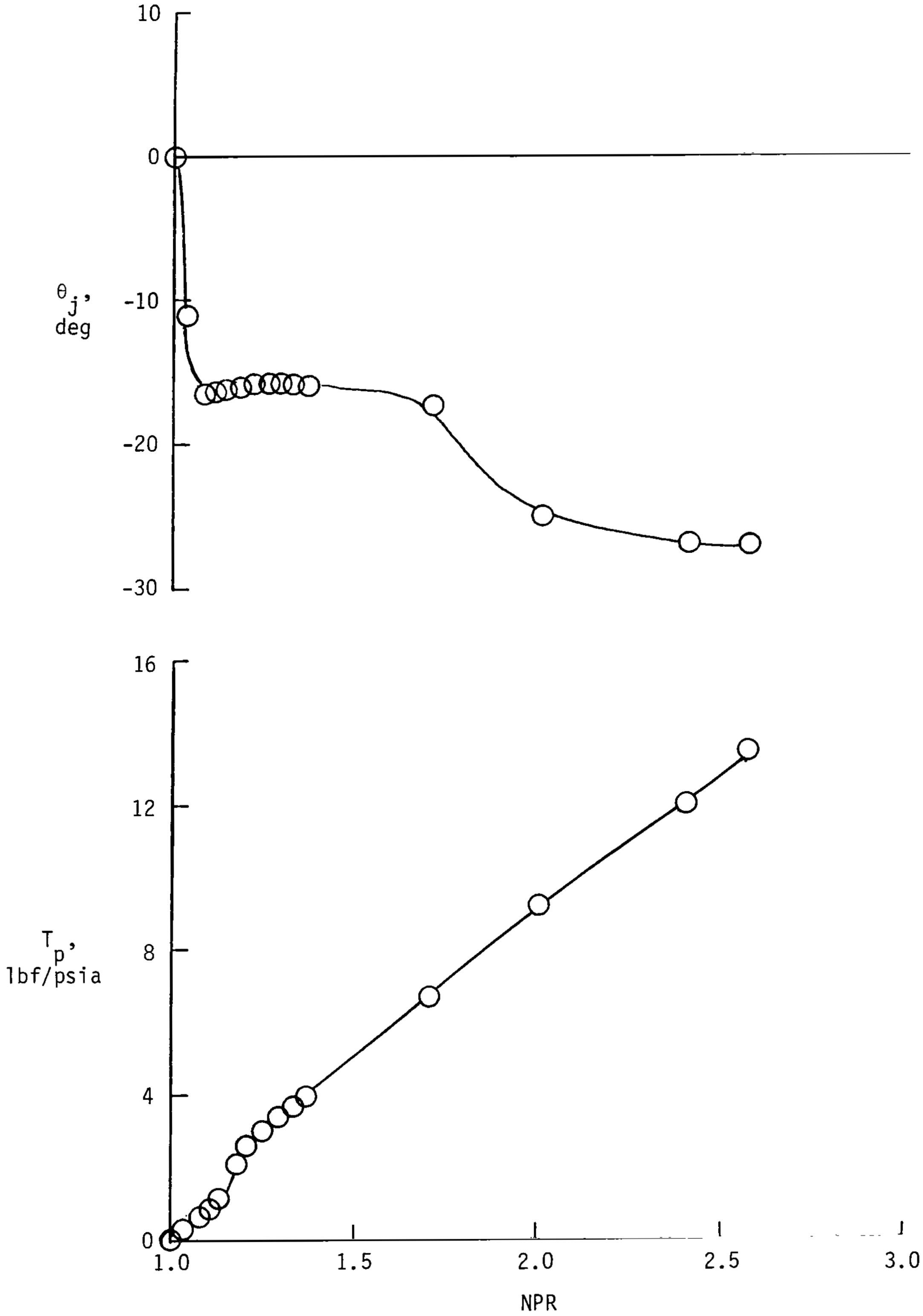

(b) Main and spanwise nozzles (Λ_s = 40°); δ_f = 30°.

Figure 7.- Concluded.

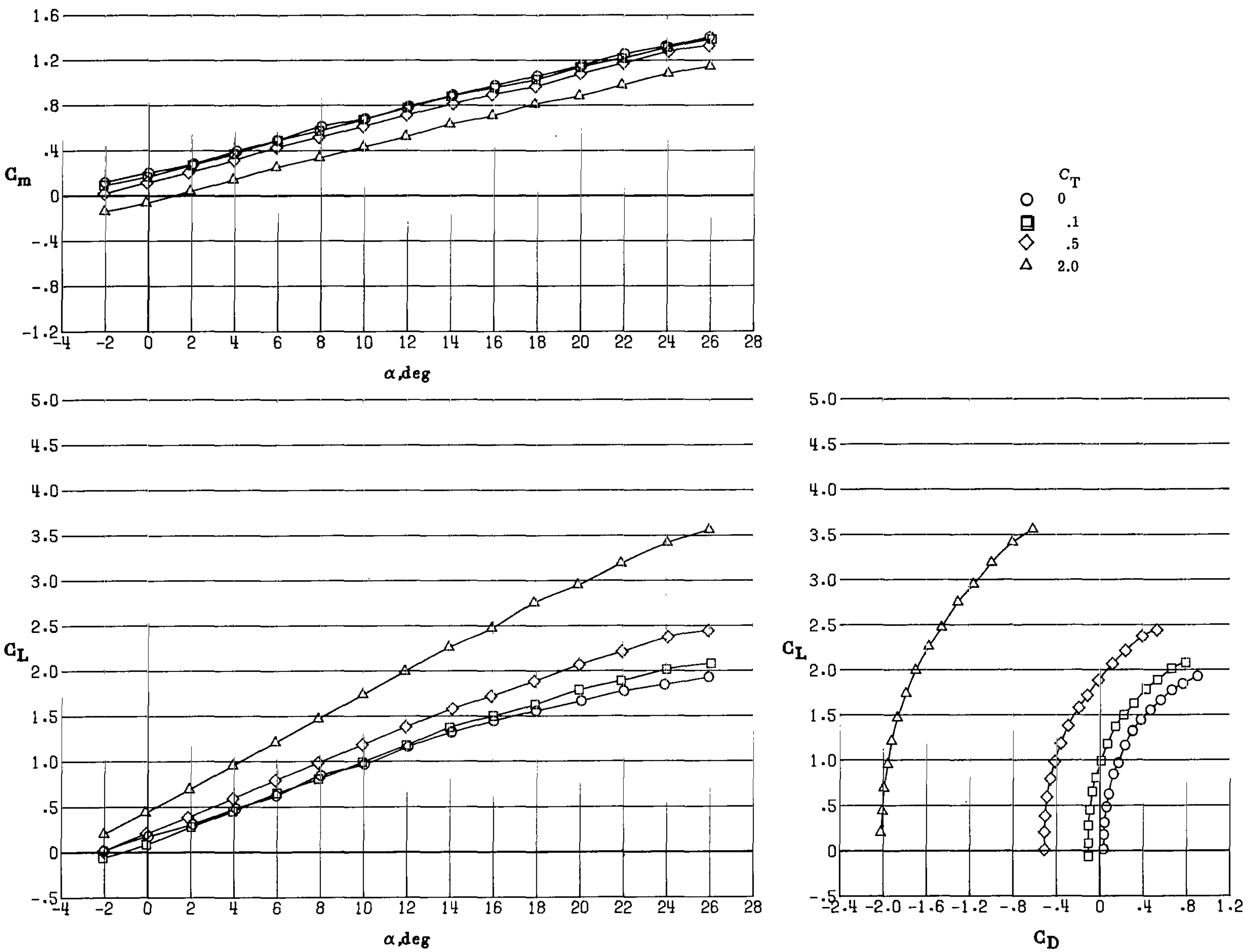

Figure 8.- Powered (total) longitudinal aerodynamic characteristics for main nozzle alone with $\delta_f = 0°$ at various thrust coefficients.

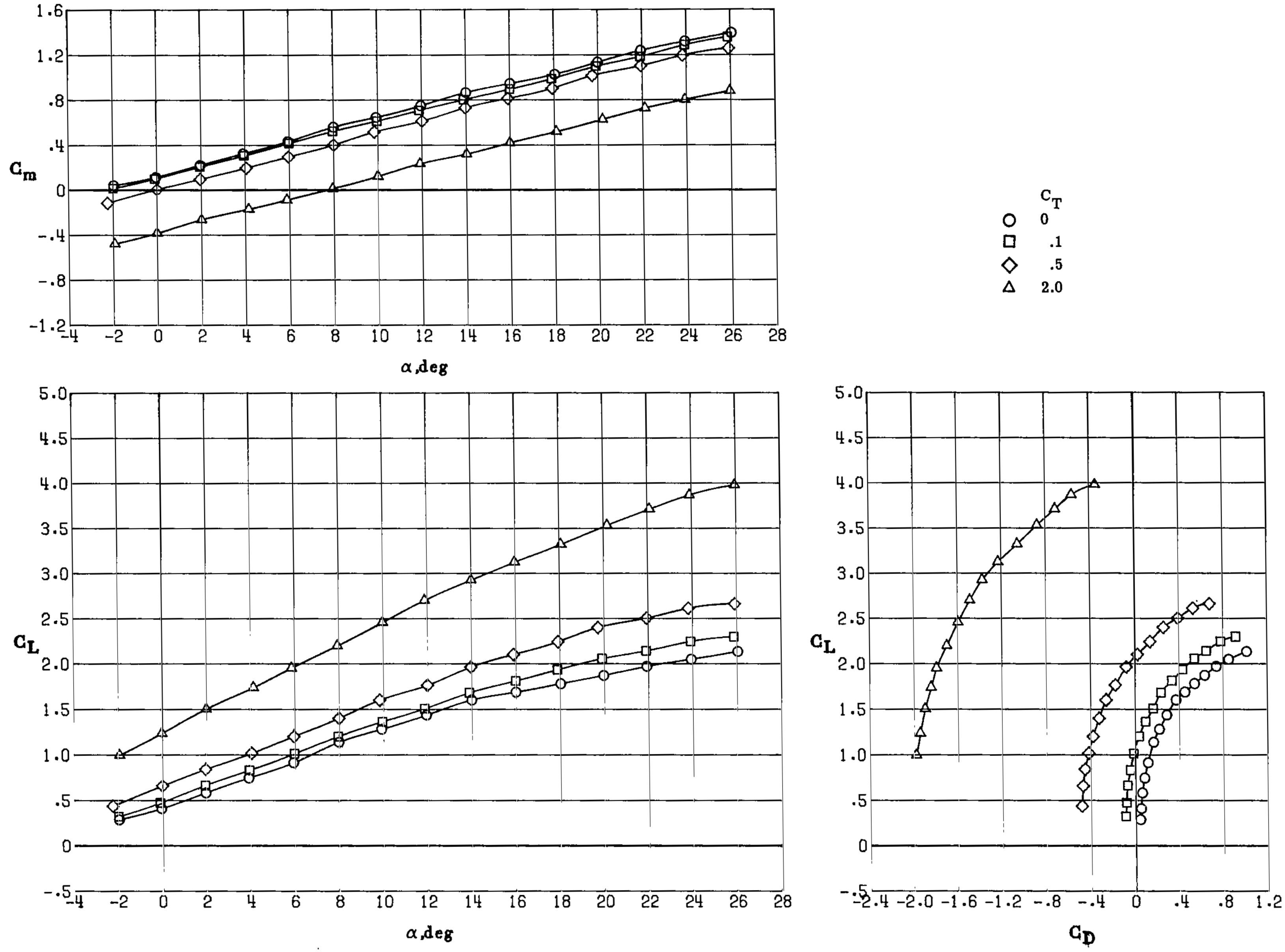

Figure 9.- Powered (total) longitudinal aerodynamic characteristics for main nozzle alone with δ_f = 15° at various thrust coefficients.

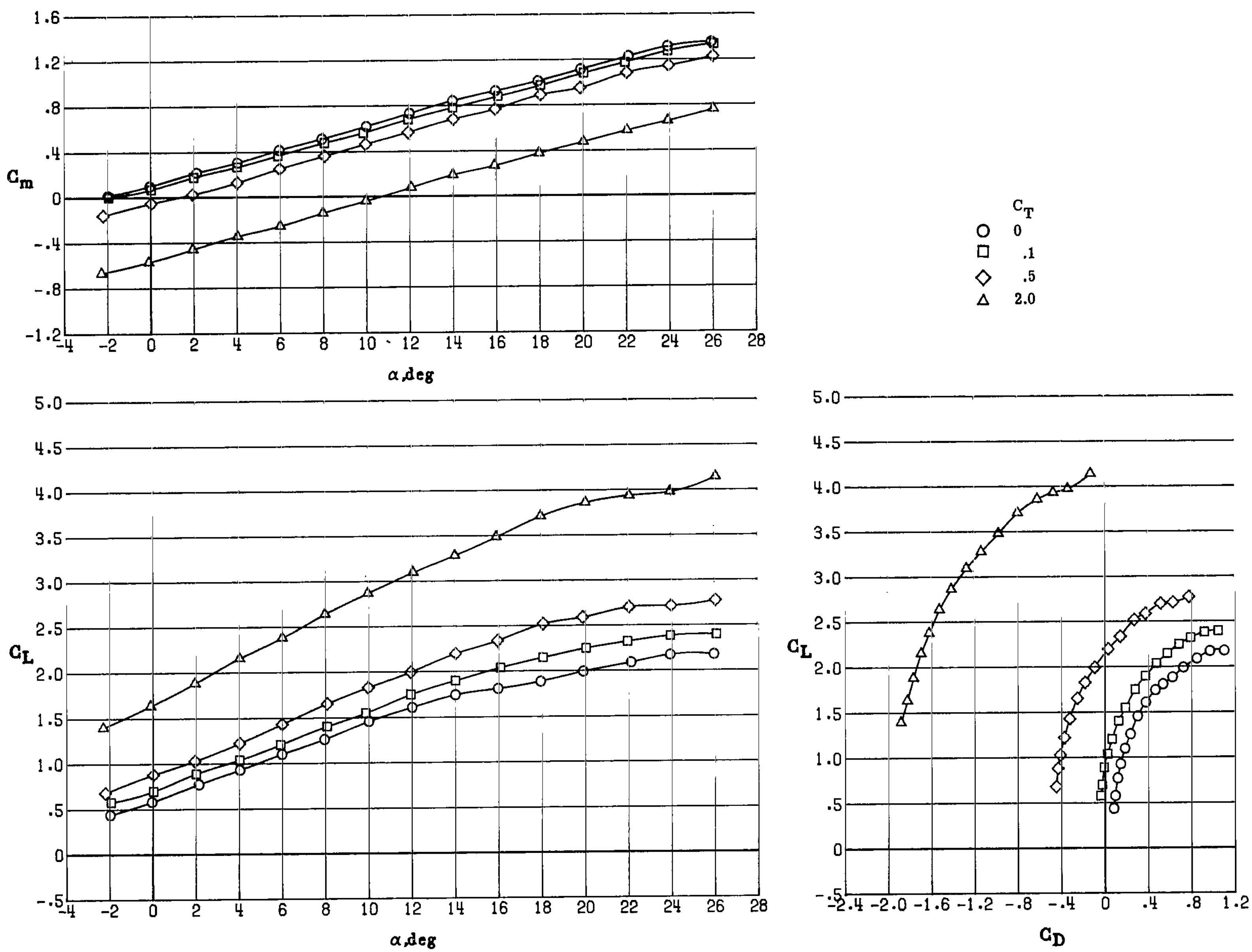

Figure 10.- Powered (total) longitudinal aerodynamic characteristics for main nozzle alone with $\delta_f = 30°$ at various thrust coefficients.

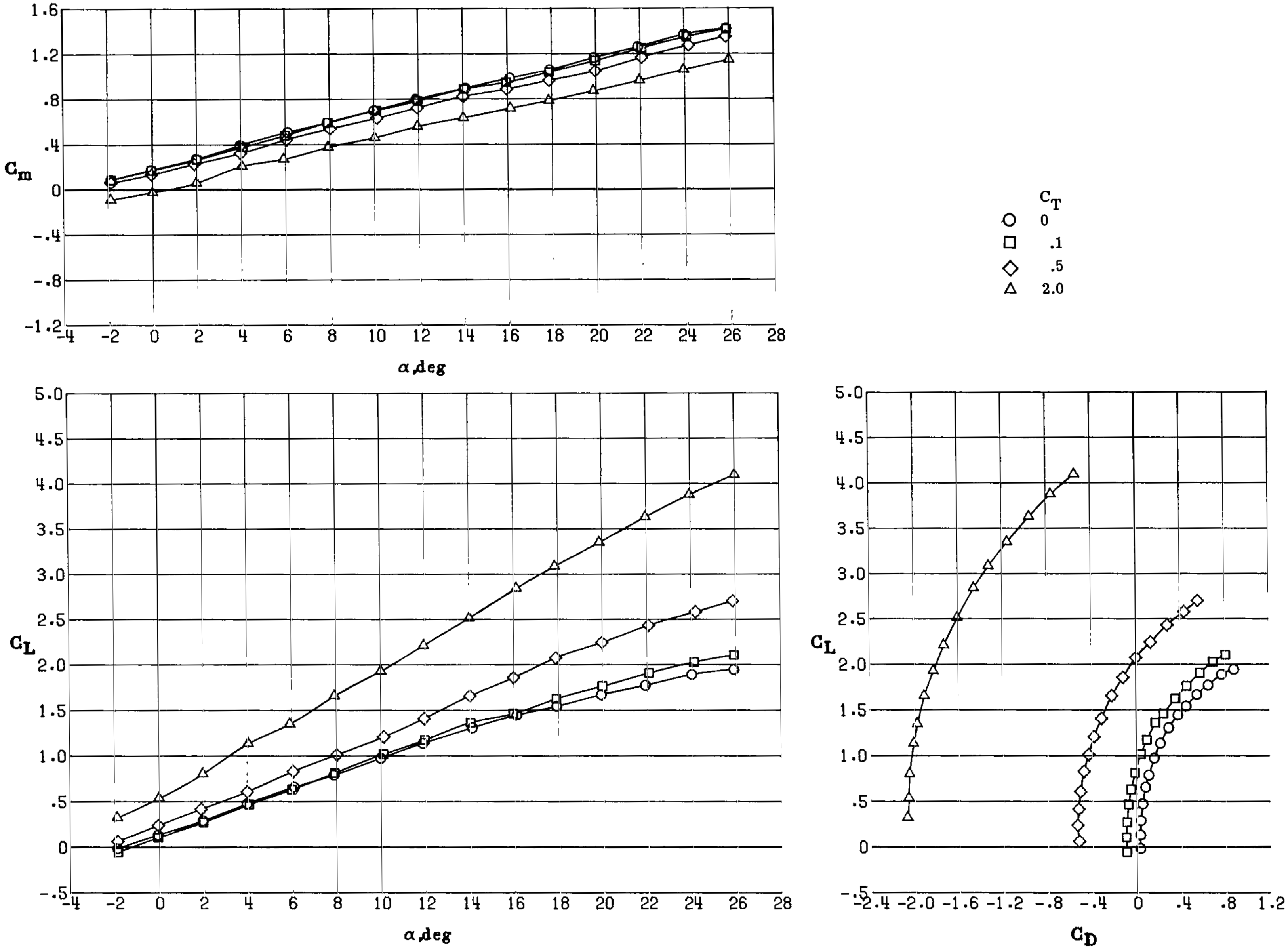

Figure 11.- Powered (total) longitudinal aerodynamic characteristics for main and 40°-sweep spanwise-blowing nozzles with $\delta_f = 0°$ at various thrust coefficients.

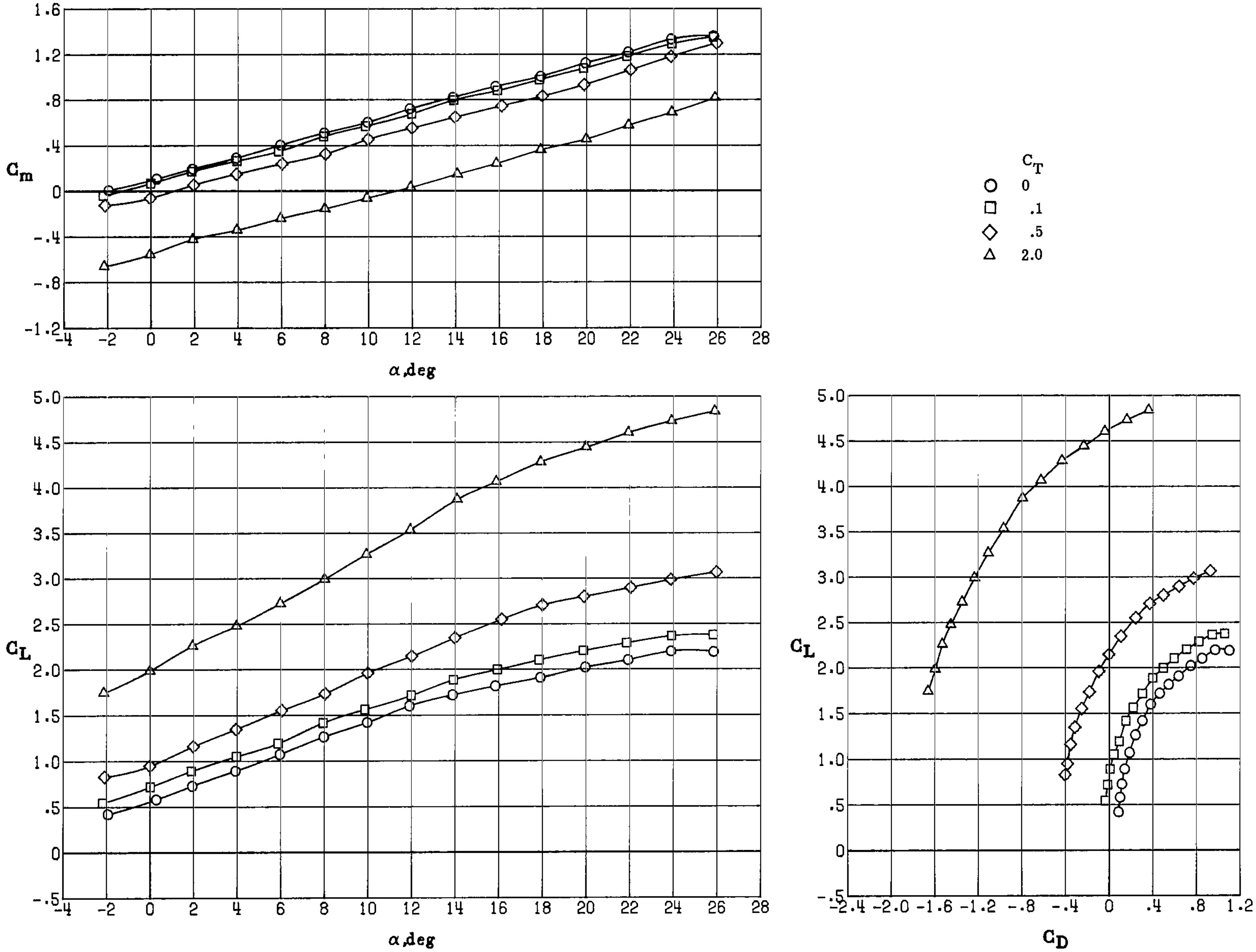

Figure 12.- Powered (total) longitudinal aerodynamic characteristics for main and 40°-sweep spanwise-blowing nozzles with δ_f = 30° at various thrust coefficients.

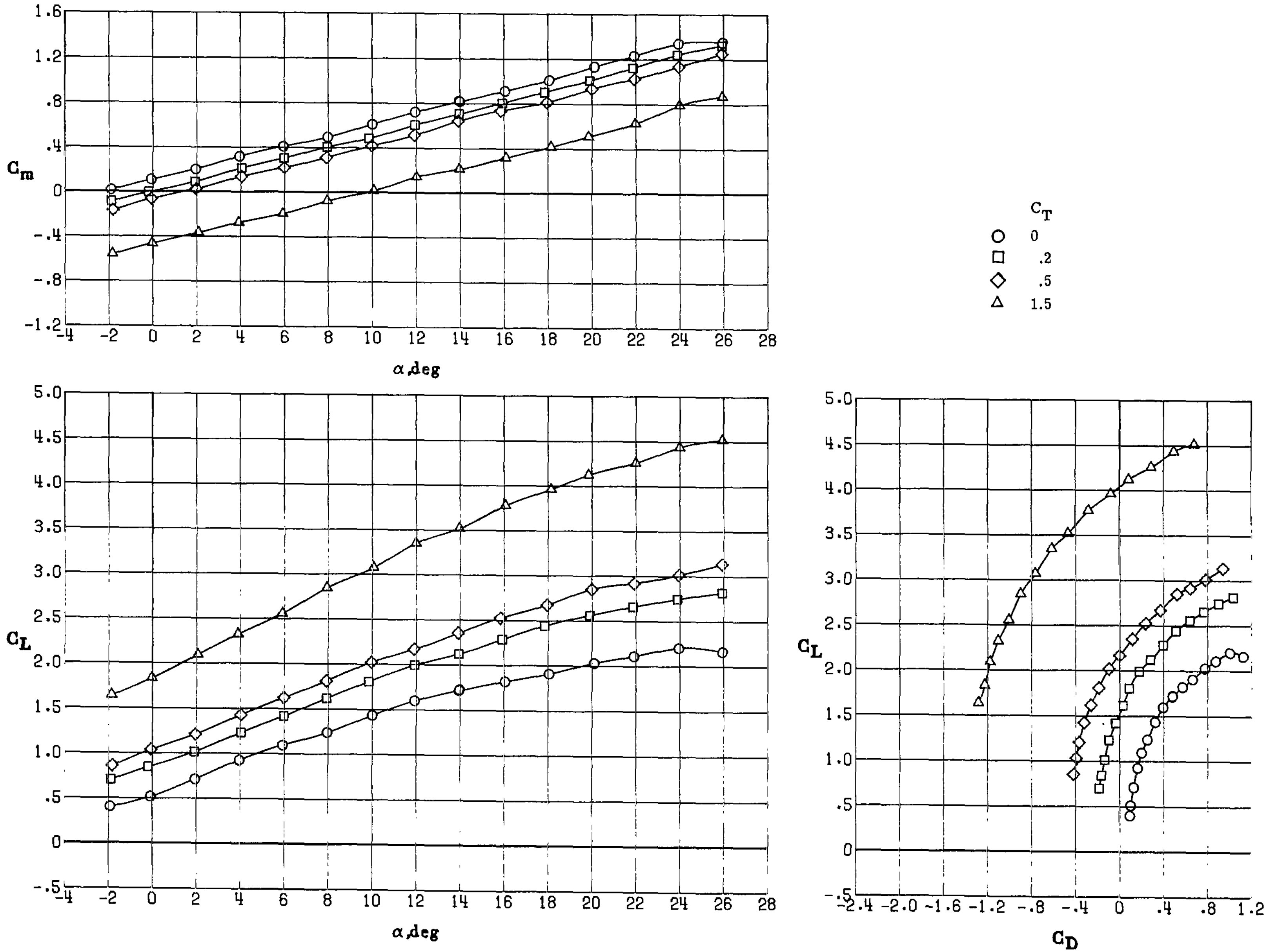

Figure 13.- Powered (total) longitudinal aerodynamic characteristics for main and 60°-sweep spanwise-blowing nozzles with $\delta_f = 30°$ at various thrust coefficients.

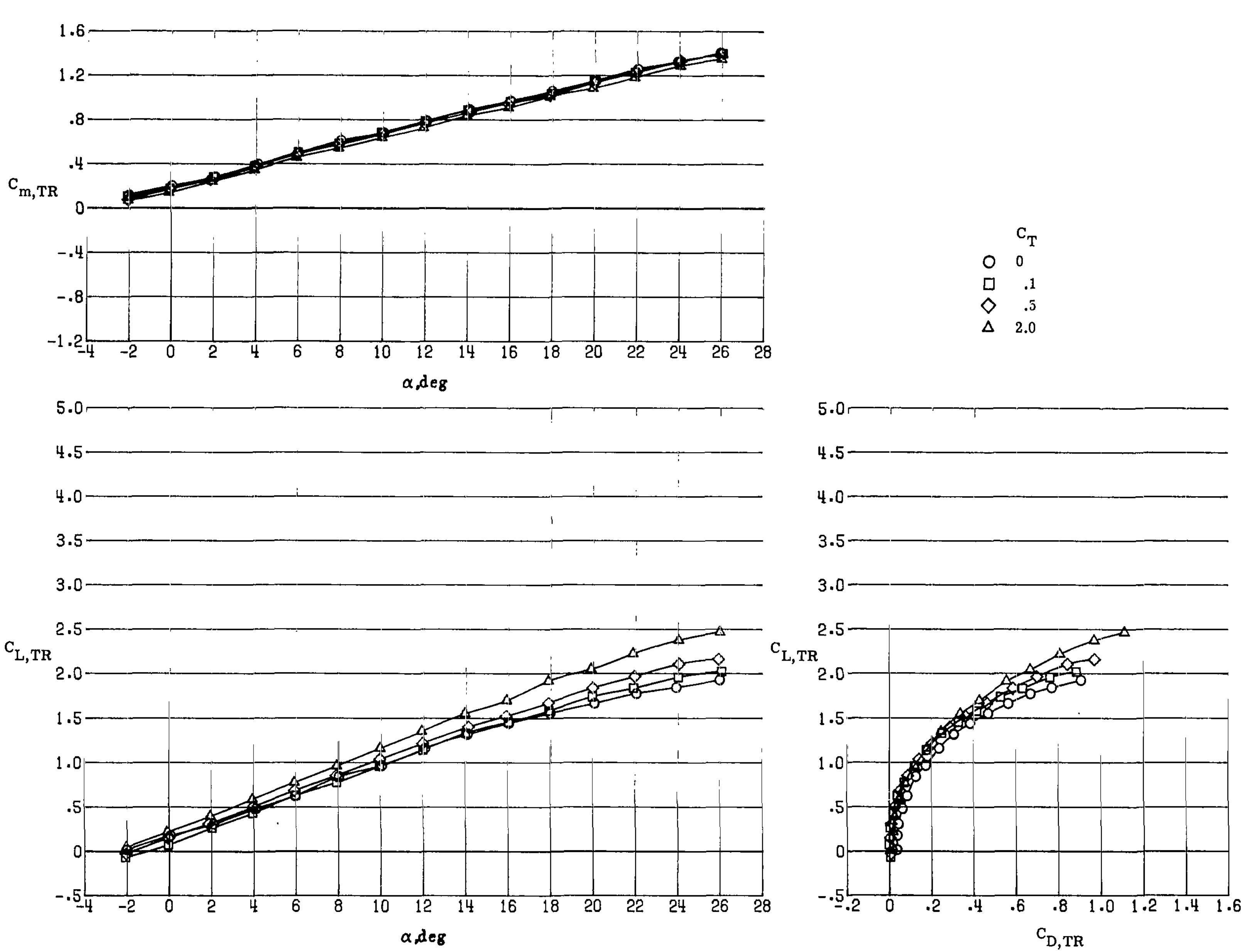

Figure 14.- Thrust-removed longitudinal aerodynamic characteristics for main nozzle alone with $\delta_f = 0°$ at various thrust coefficients.

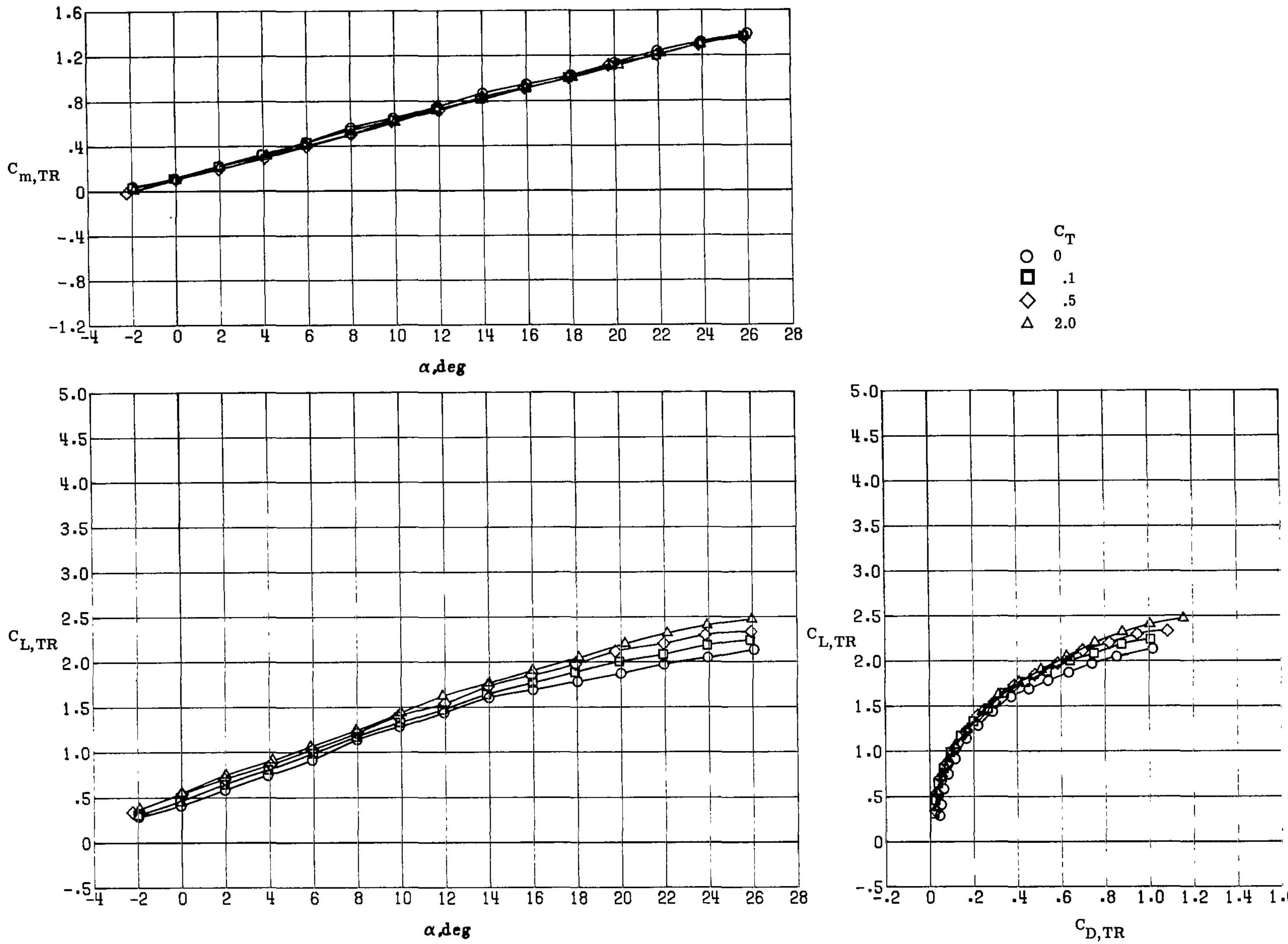

Figure 15.- Thrust-removed longitudinal aerodynamic characteristics for main nozzle alone with δ_f = 15° at various thrust coefficients.

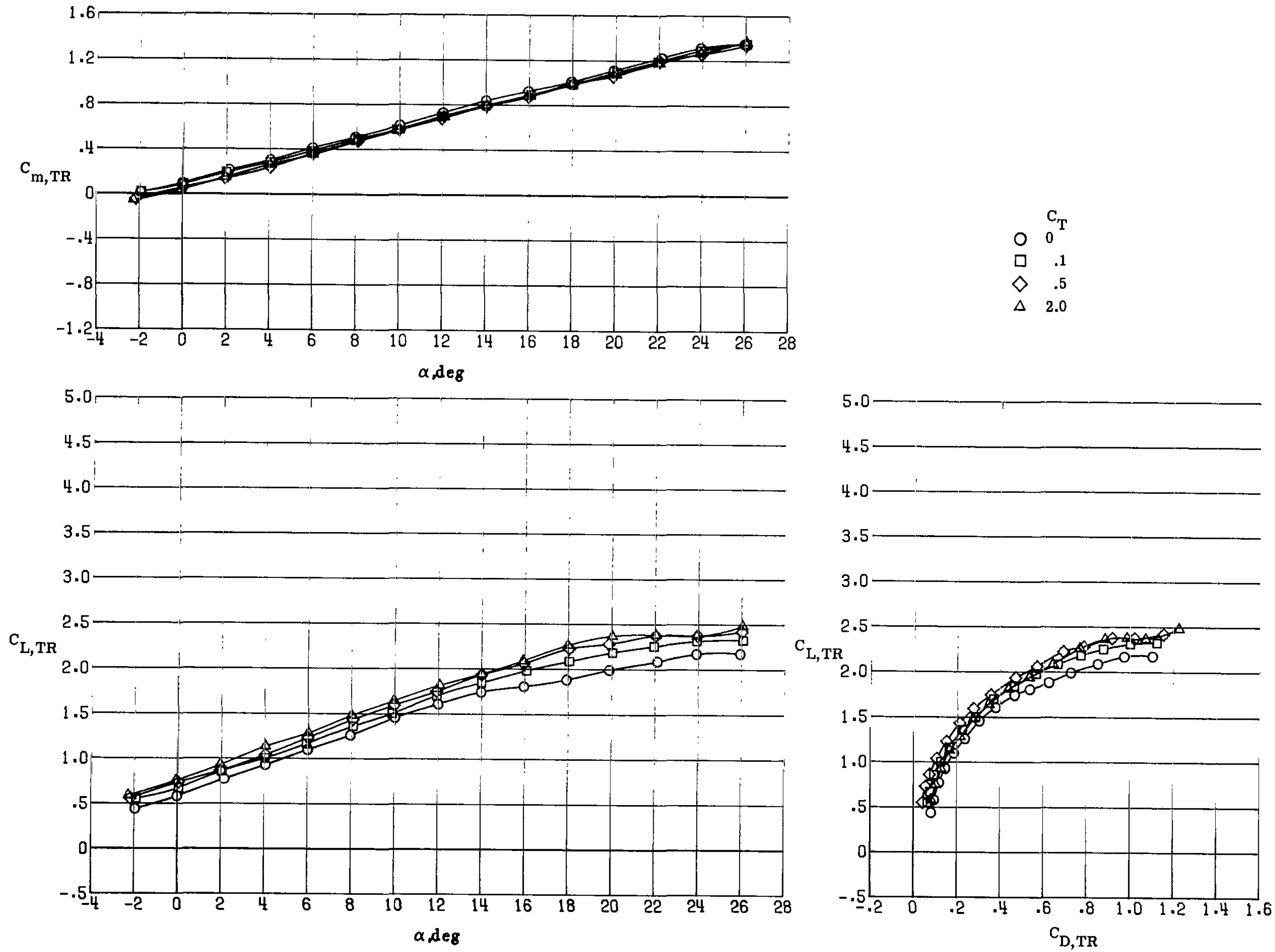

Figure 16.- Thrust-removed longitudinal aerodynamic characteristics for main nozzle alone with $\delta_f = 30°$ at various thrust coefficients.

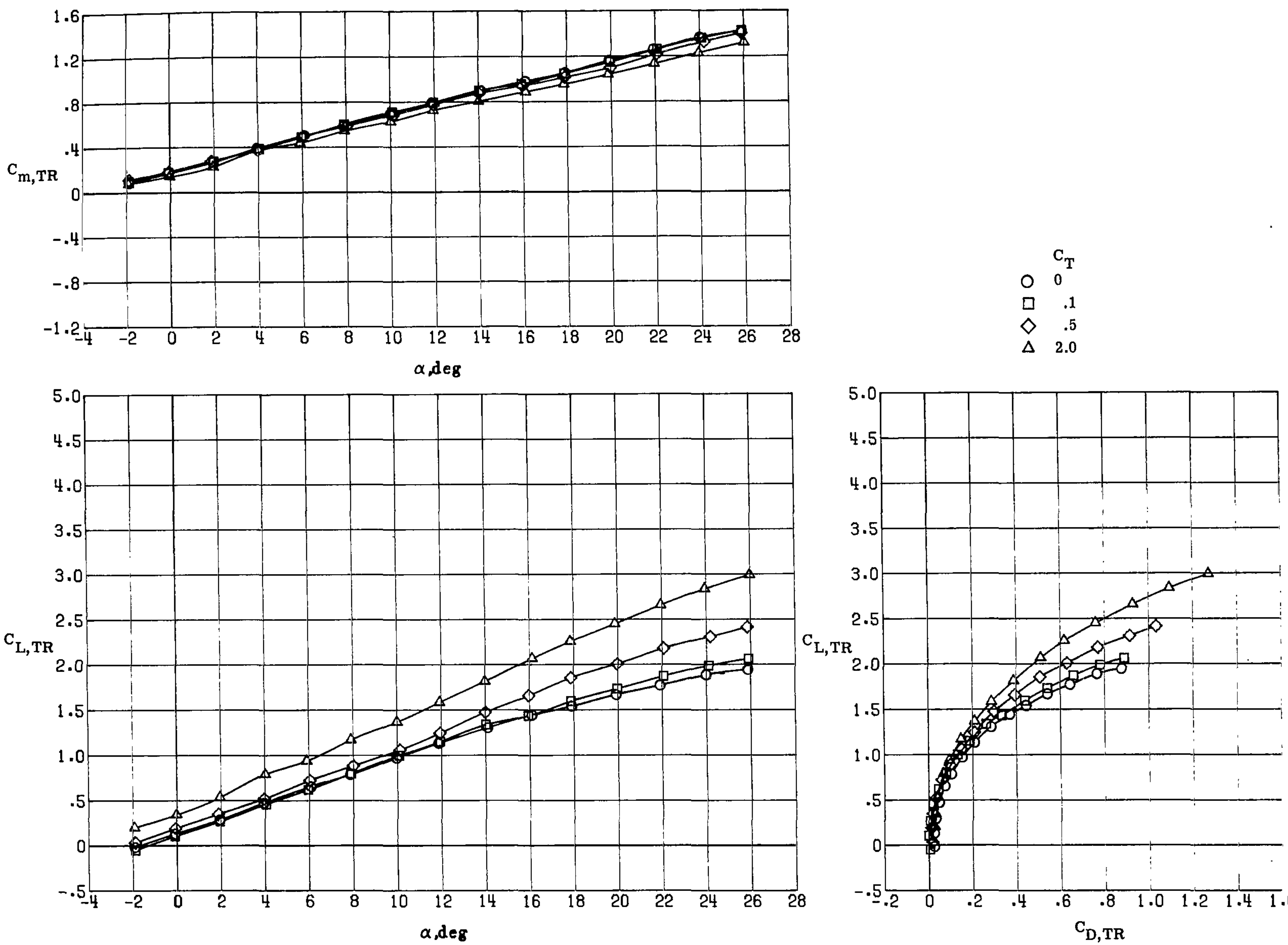

Figure 17.- Thrust-removed longitudinal aerodynamic characteristics for main and 40°-sweep spanwise-blowing nozzles with $\delta_f = 0°$ at various thrust coefficients.

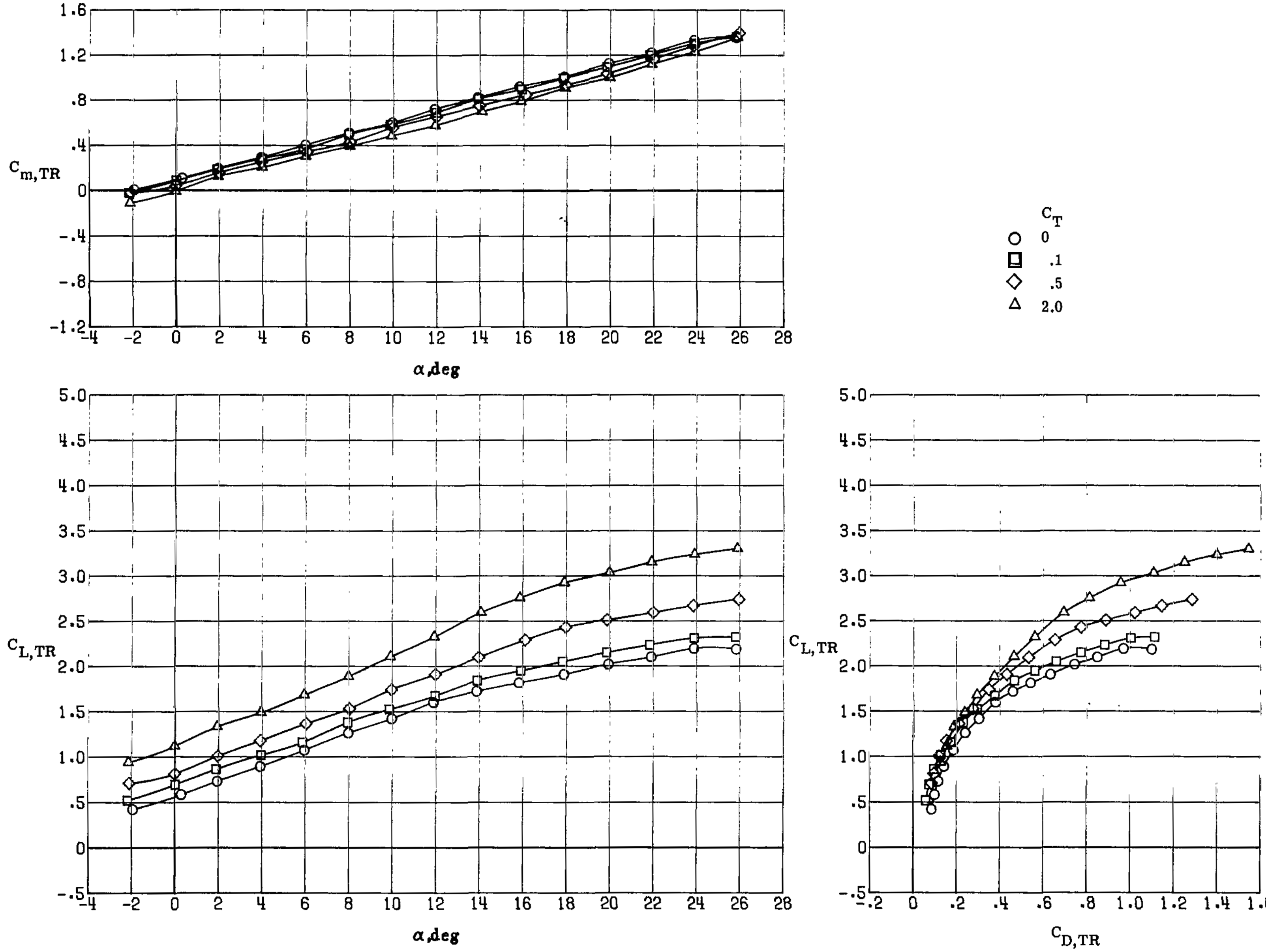

Figure 18.- Thrust-removed longitudinal aerodynamic characteristics for main and 40°-sweep spanwise-blowing nozzles with $\delta_f = 30°$ at various thrust coefficients.

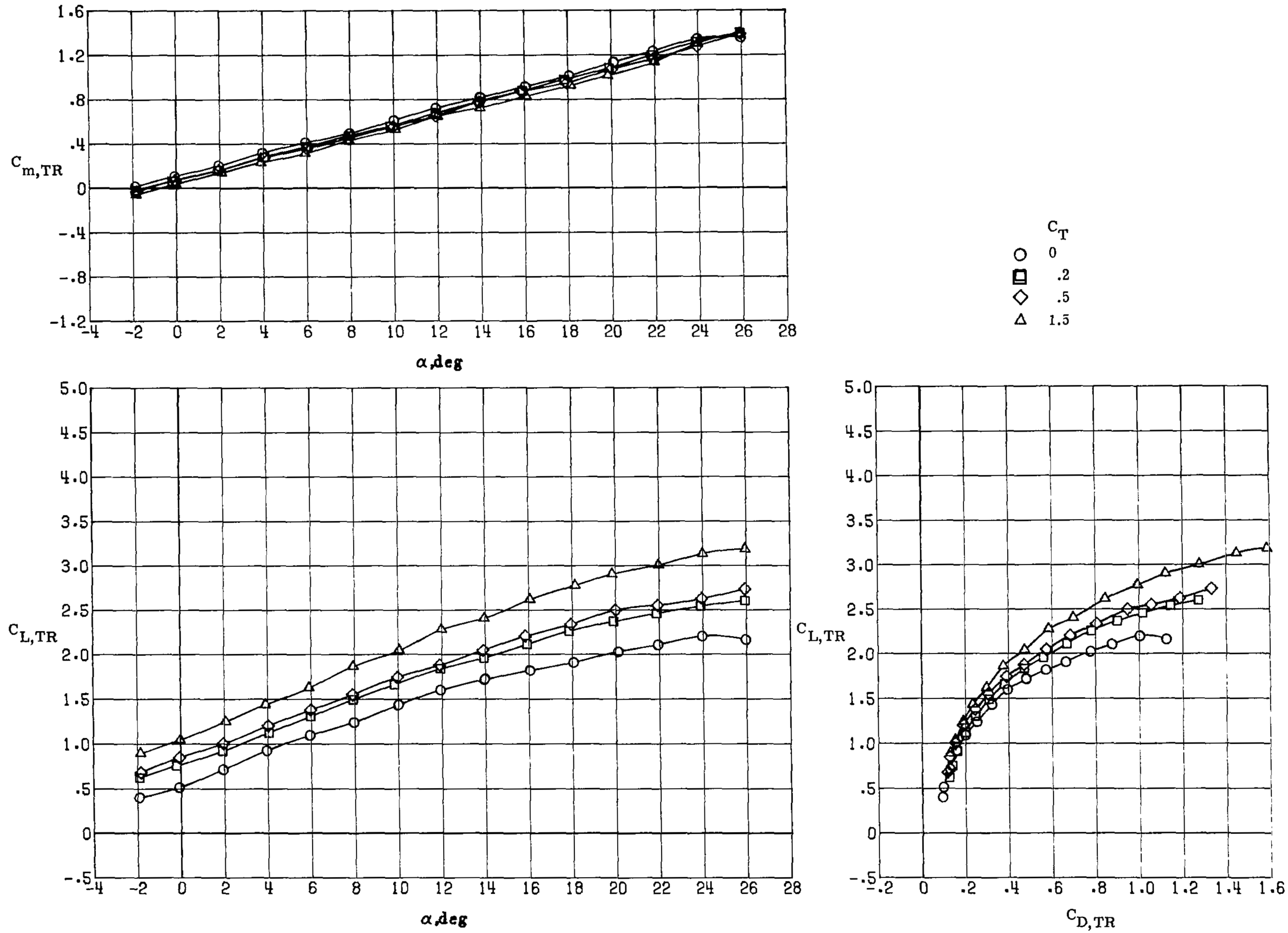

Figure 19.- Thrust-removed longitudinal aerodynamic characteristics for main and 60°-sweep spanwise-blowing nozzles with $\delta_f = 30°$ at various thrust coefficients.

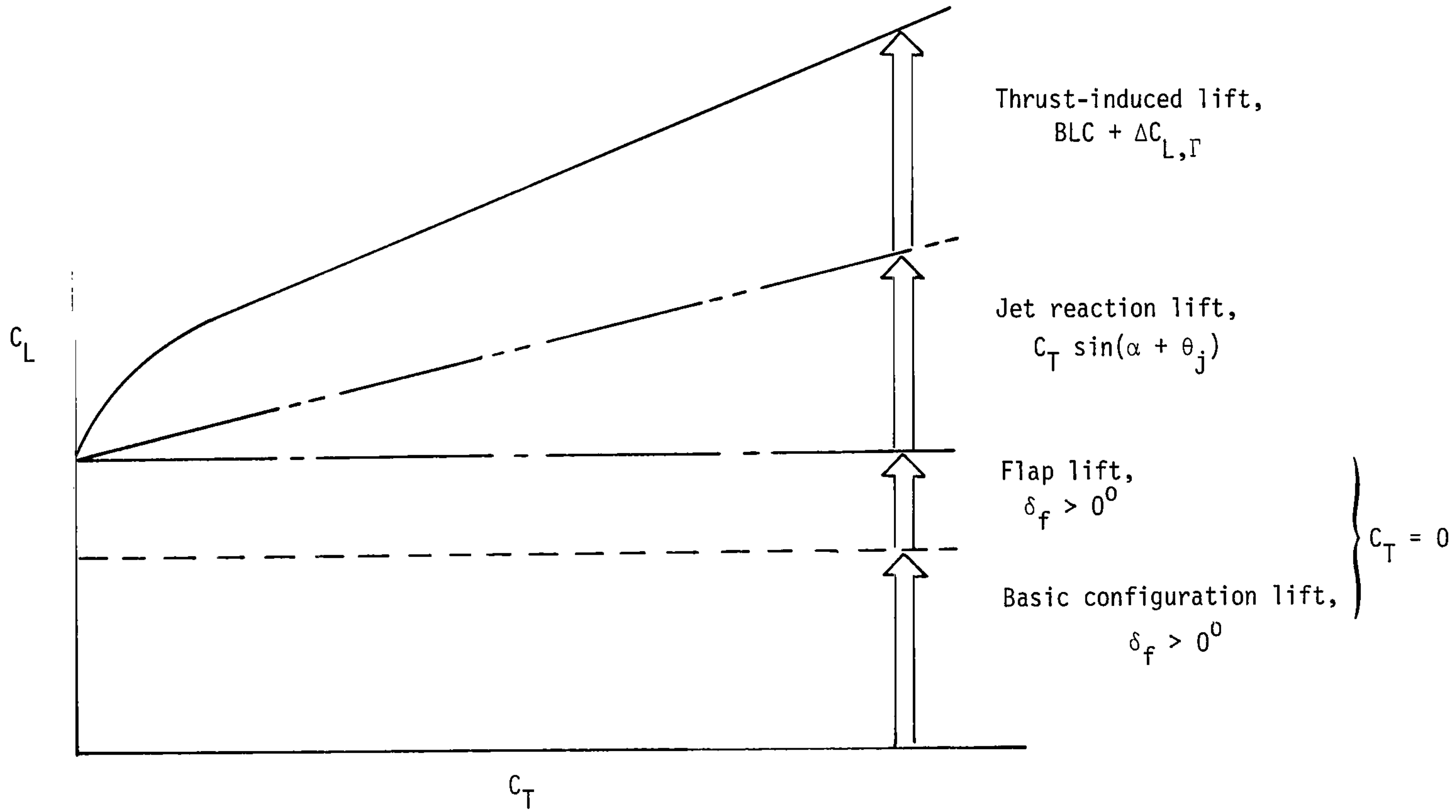

Figure 20.- Components of powered lift at a constant angle of attack.

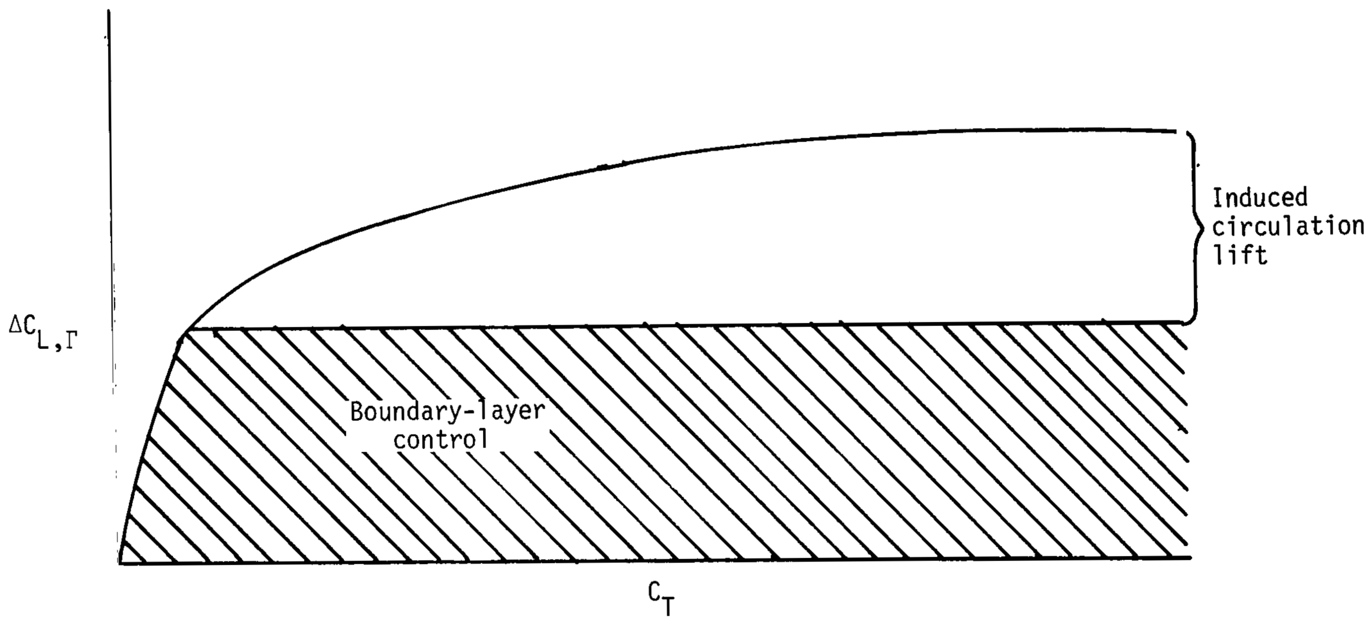

Figure 21.- Components of thrust-induced lift for $\alpha > 0°$.

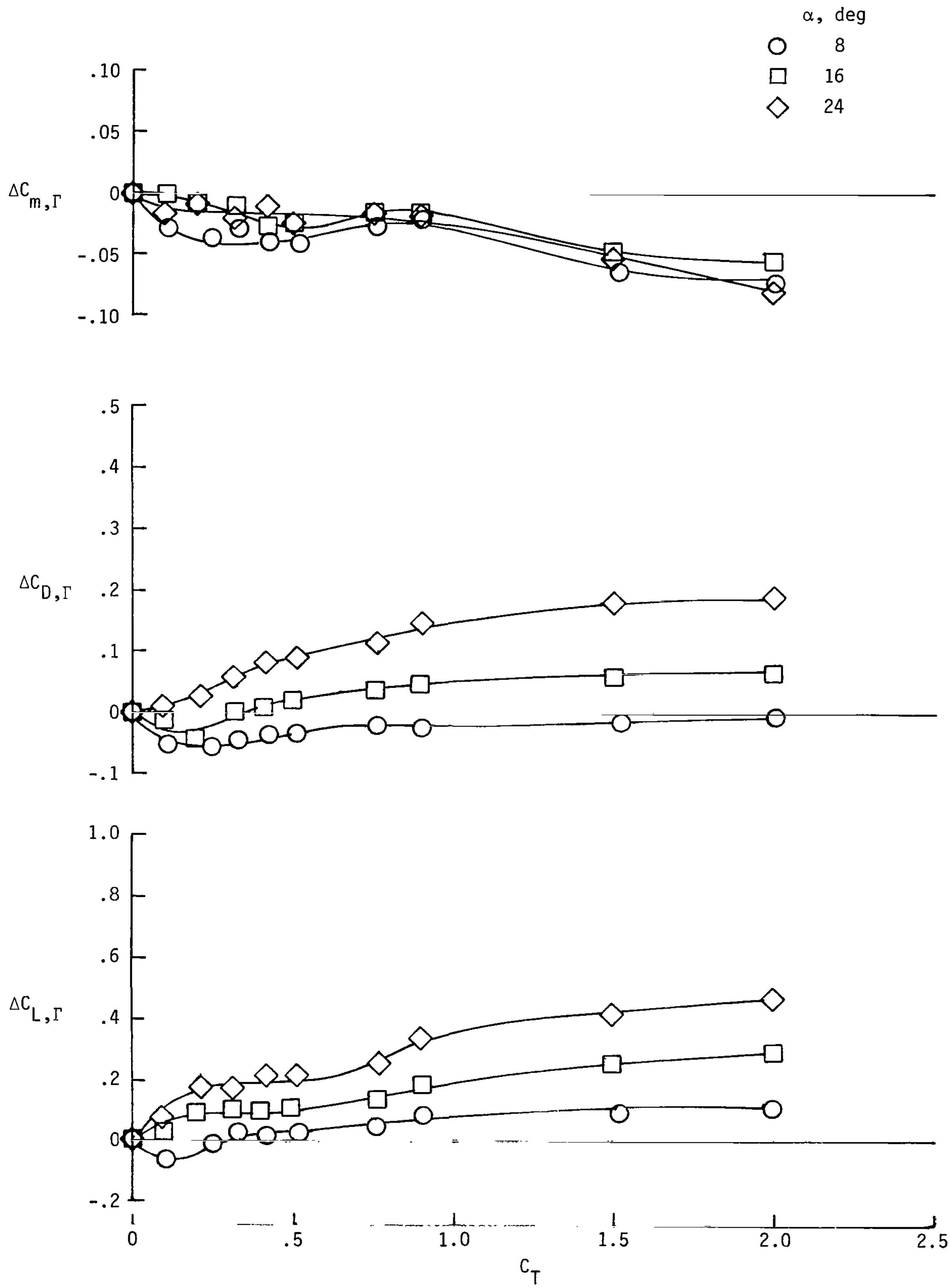

Figure 22.- Thrust-induced longitudinal aerodynamic characteristics for main nozzle alone with $\delta_f = 0°$ at various angles of attack.

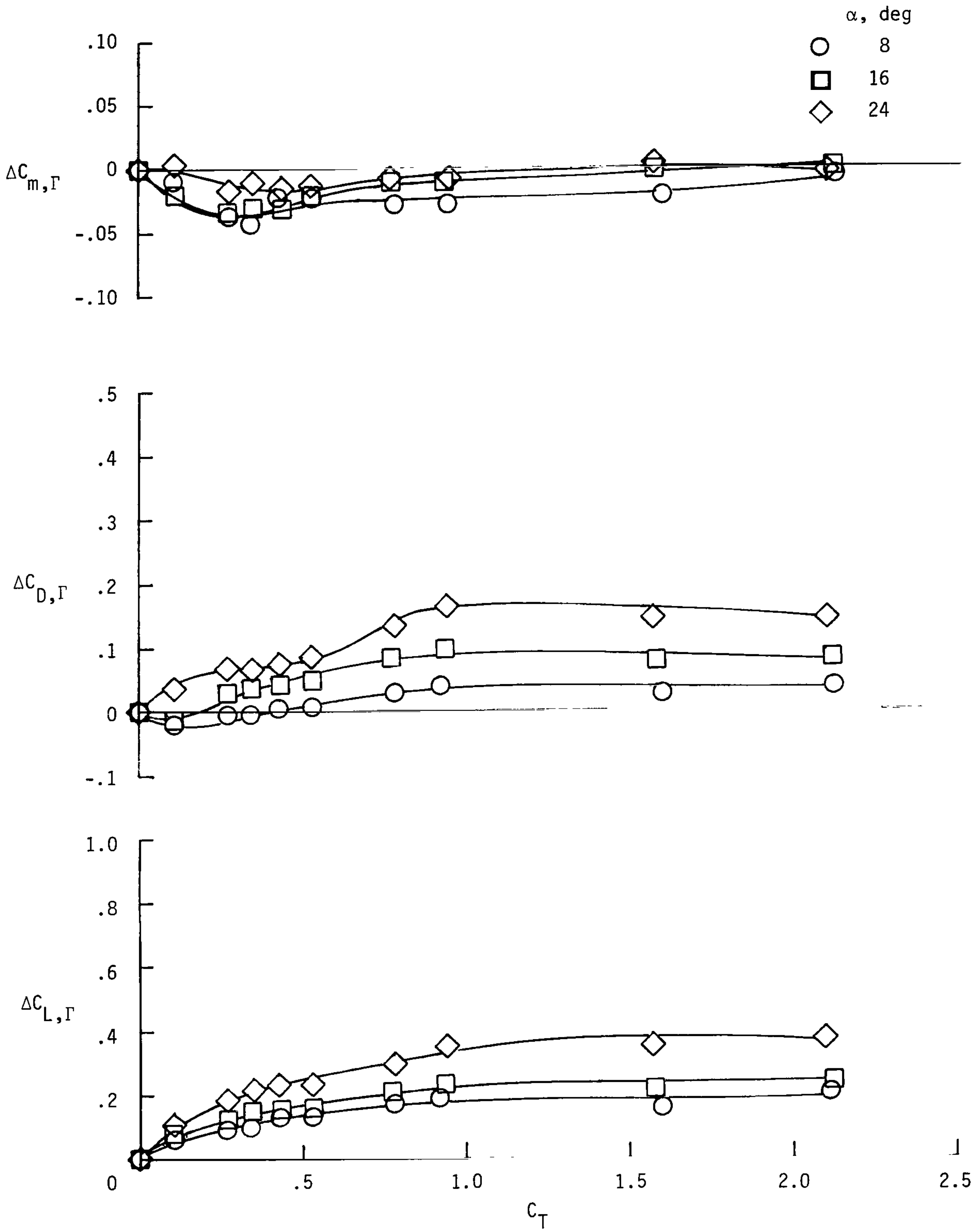

Figure 23.- Thrust-induced longitudinal aerodynamic characteristics for the main nozzle alone with δ_f = 15° at various angles of attack.

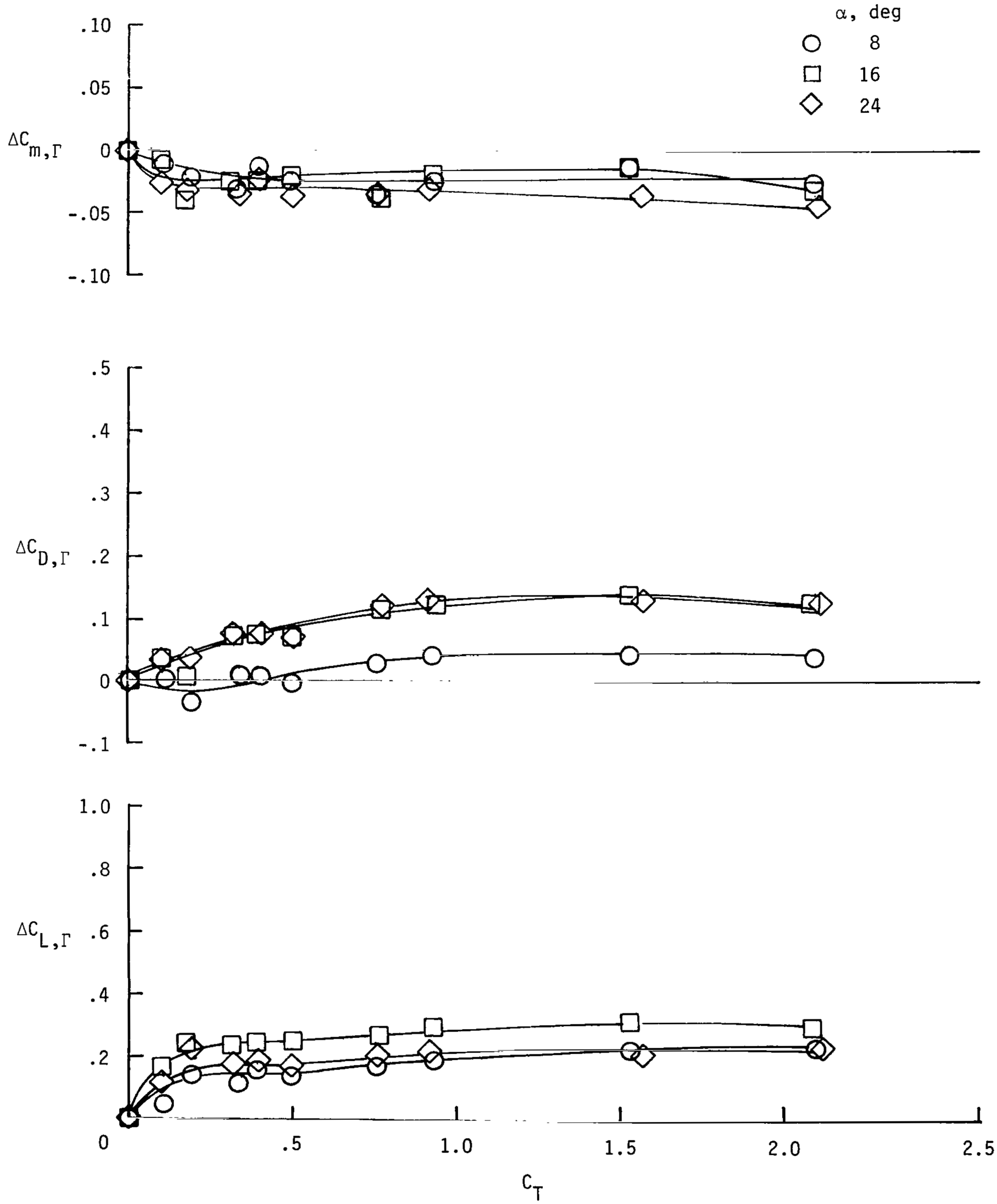

Figure 24.- Thrust-induced longitudinal aerodynamic characteristics for main nozzle alone with $\delta_f = 30°$ at various angles of attack.

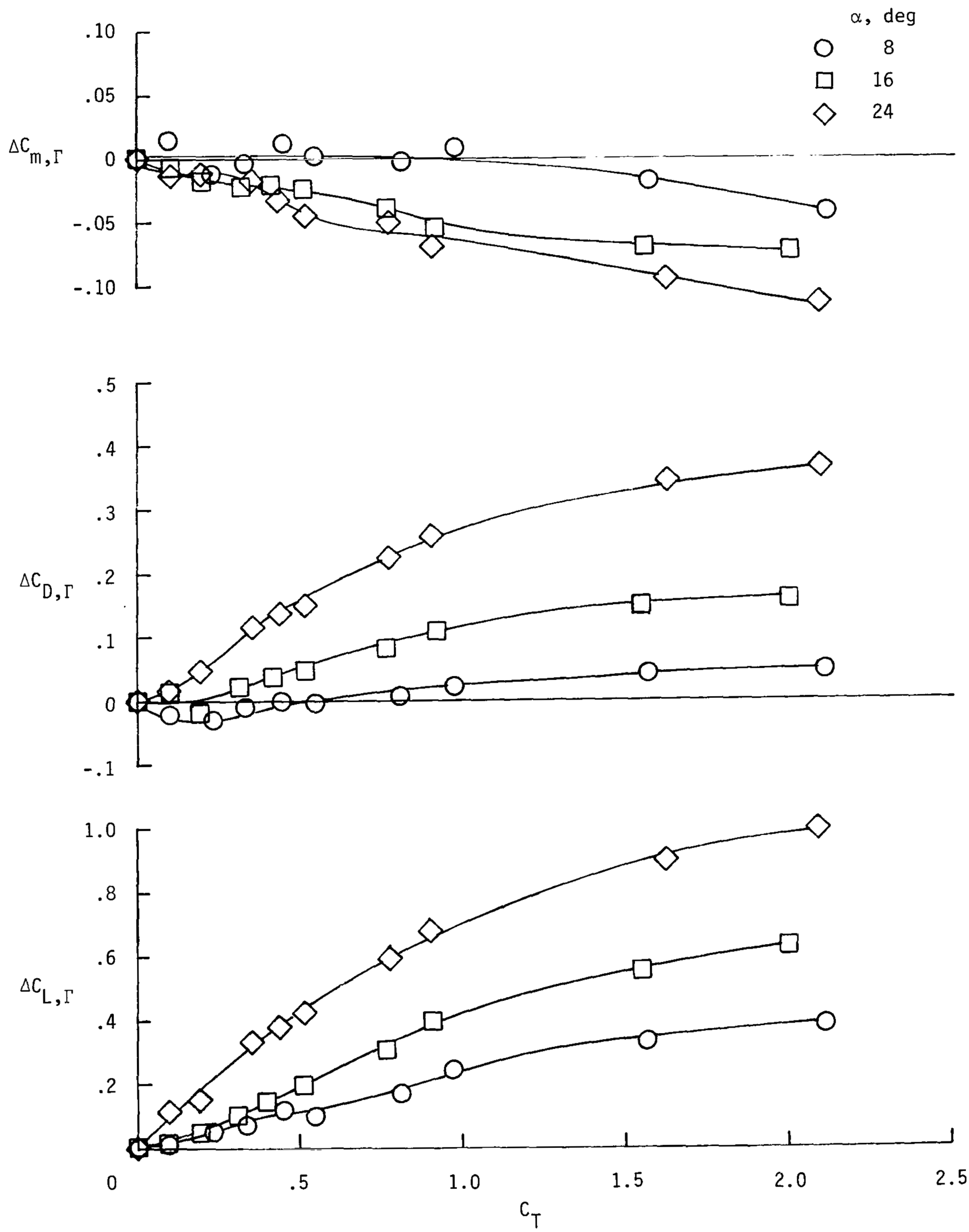

Figure 25.- Thrust-induced longitudinal aerodynamic characteristics for main and 40°-sweep spanwise-blowing nozzles with $\delta_f = 0°$ at various angles of attack.

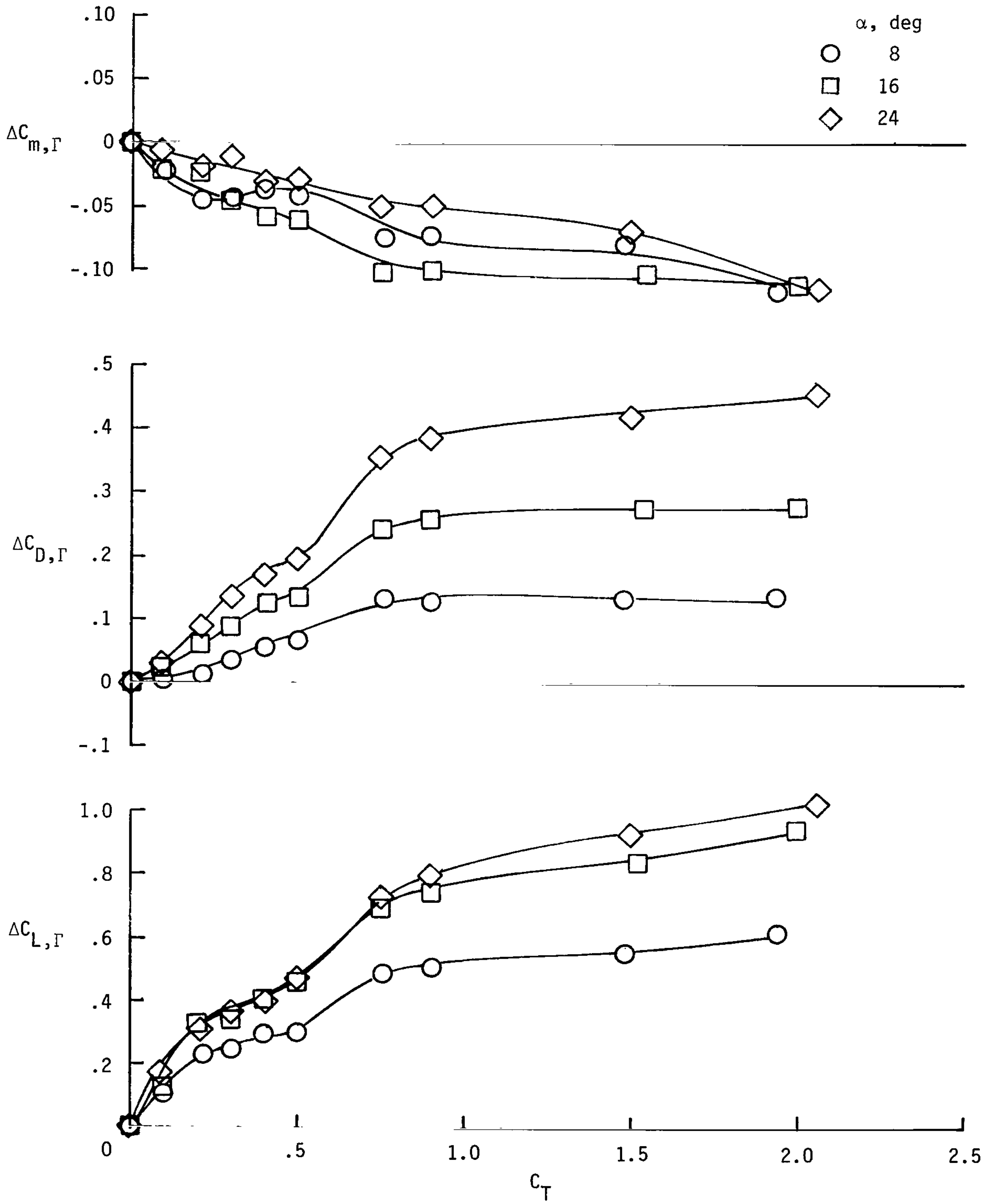

Figure 26.- Thrust-induced longitudinal aerodynamic characteristics for main and 40°-sweep spanwise-blowing nozzles with $\delta_f = 30°$ at various angles of attack.

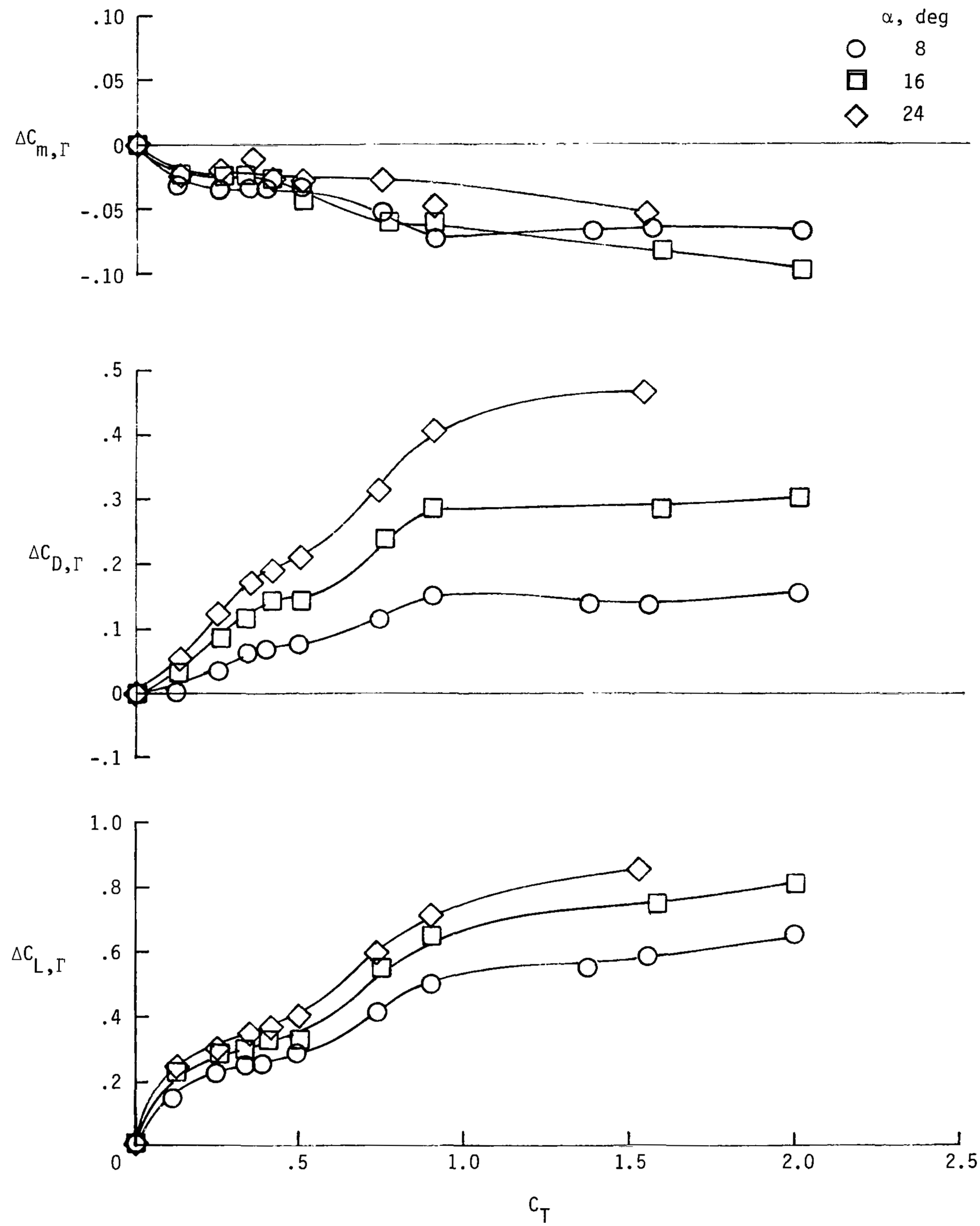

Figure 27.- Thrust-induced longitudinal aerodynamic characteristics for main and 60°-sweep spanwise-blowing nozzles with δ_f = 30° at various angles of attack.

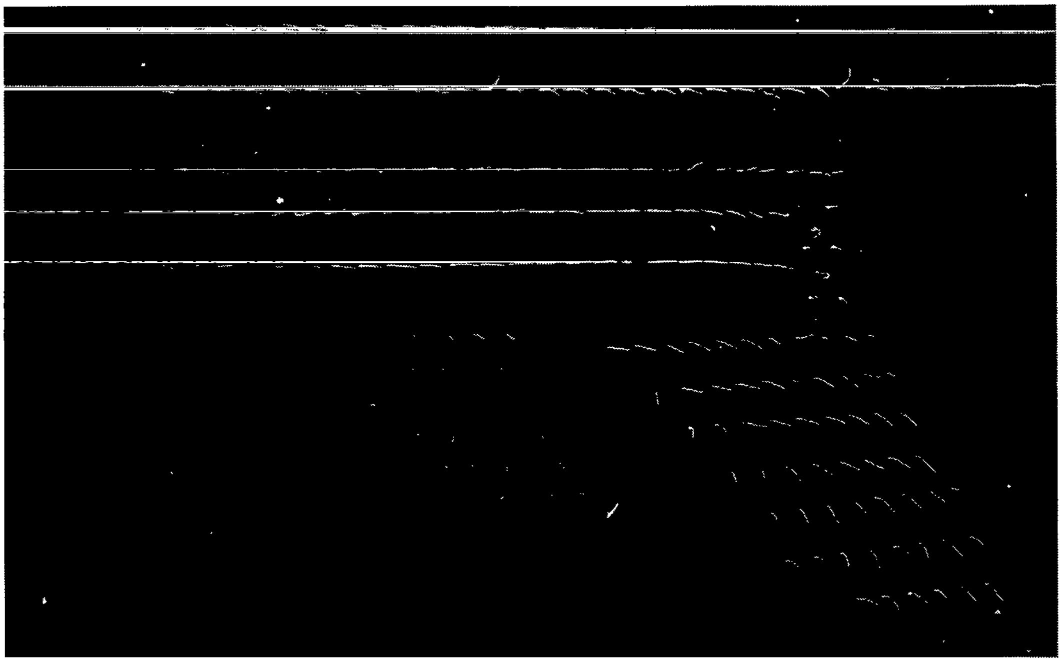

(a) $C_T = 0.$

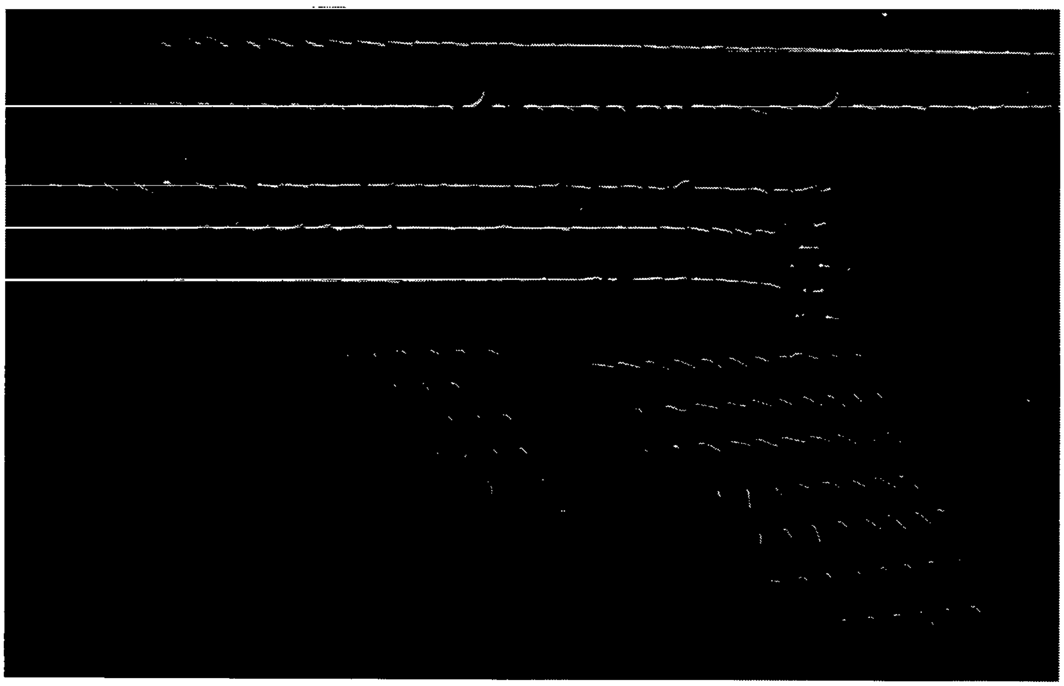

(b) $C_T = 0.2.$

L-83-117

Figure 28.- Minituft flow visualization of main nozzle alone for VEO-wing configuration with $\delta_f = 0°$ and $\alpha = 16°$.

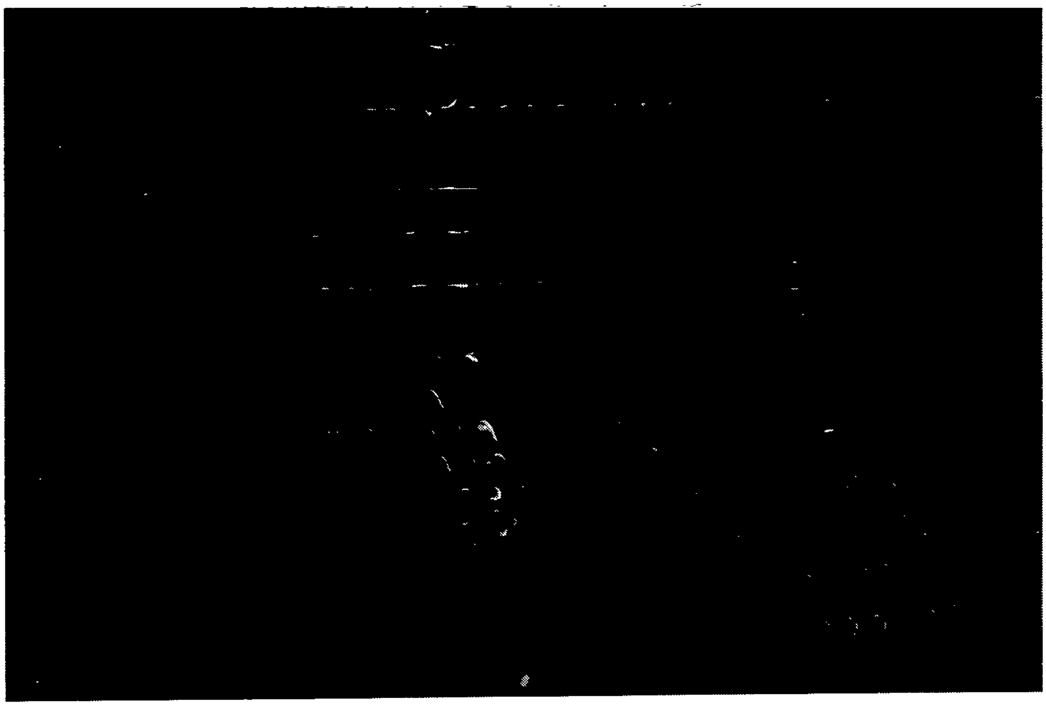

(c) $C_T = 0.9$.

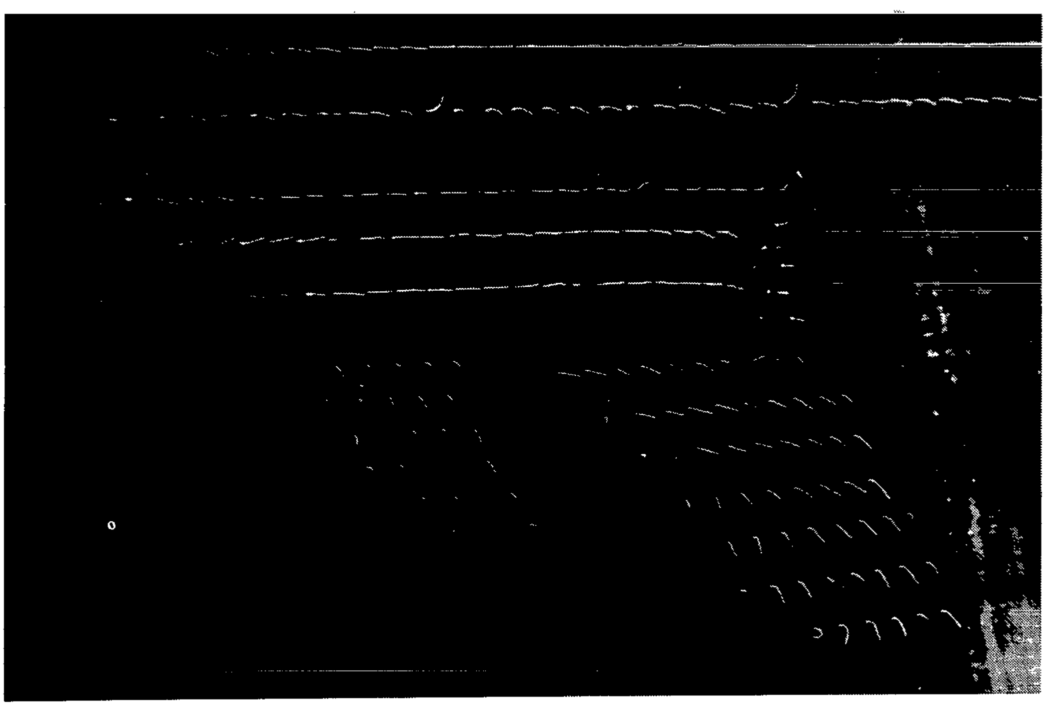

(d) $C_T = 1.5$. L-83-118

Figure 28.- Concluded.

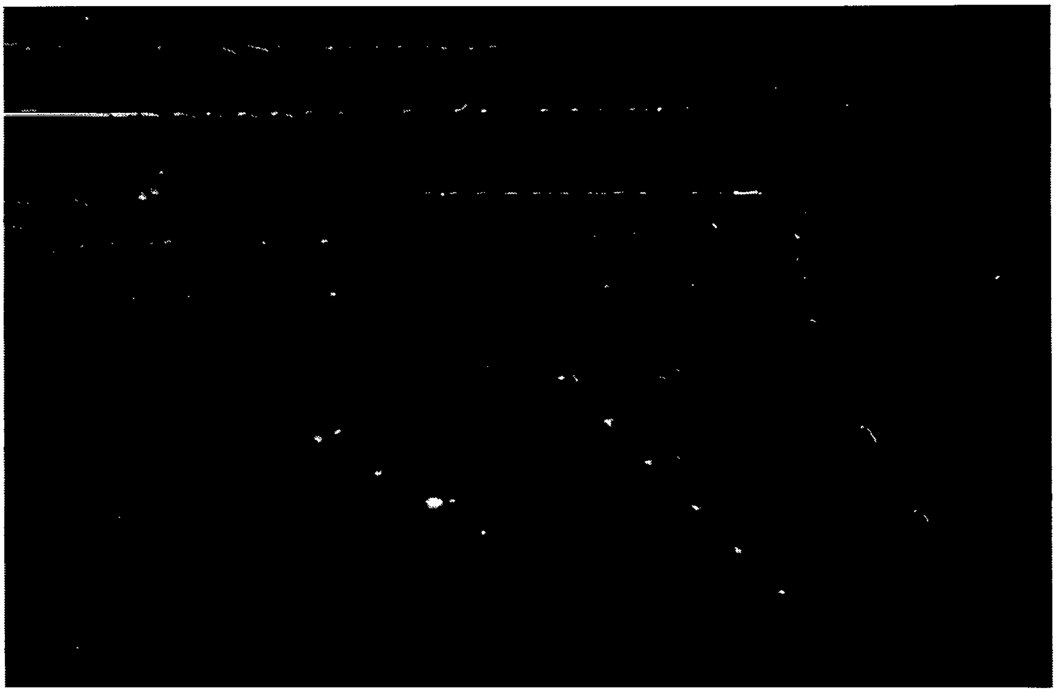

(a) $C_T = 0$.

(b) $C_T = 0.2$.

L-83-119

Figure 29.- Minituft flow visualization of main nozzle alone for VEO-wing configuration with $\delta_f = 30°$ and $\alpha = 16°$.

(c) $C_T = 0.9.$

(d) $C_T = 1.5.$

L-83-120

Figure 29.- Concluded.

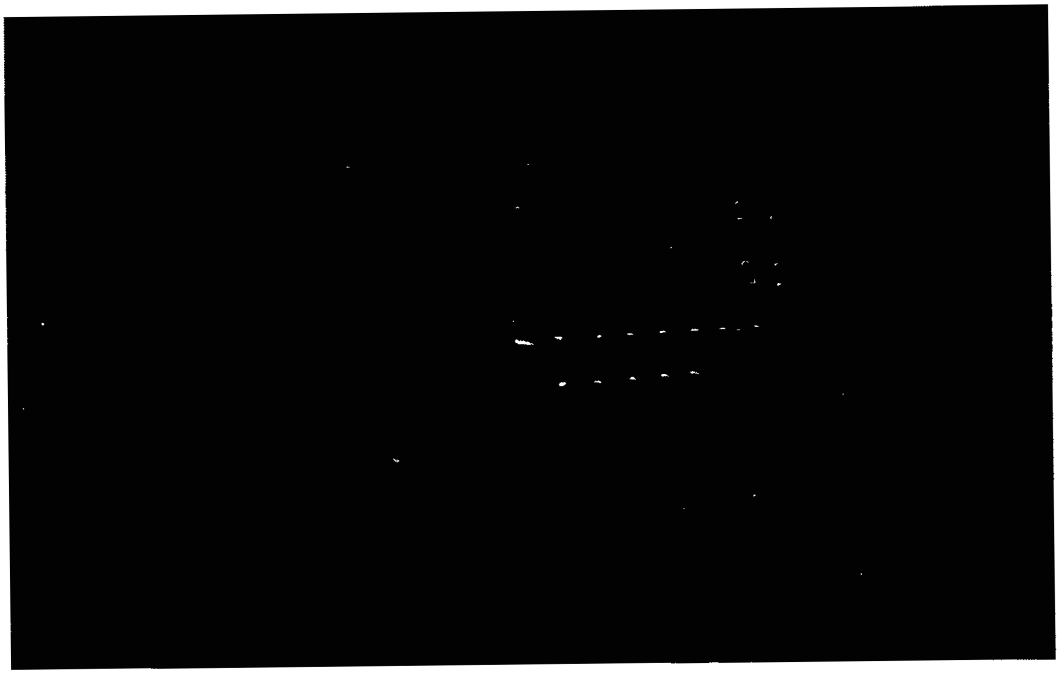

(a) $C_T = 0.$

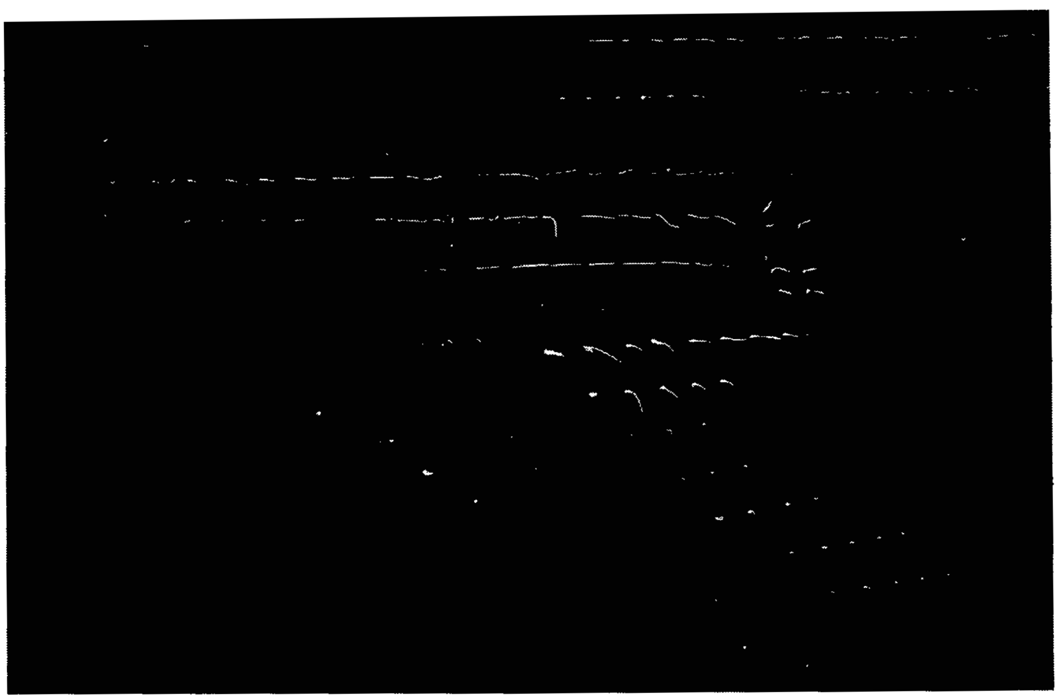

(b) $C_T = 0.2.$

L-83-121

Figure 30.- Minituft flow visualization of main and 40°-sweep spanwise-blowing nozzles for VEO-wing configuration with $\delta_f = 0°$ and $\alpha = 16°$.

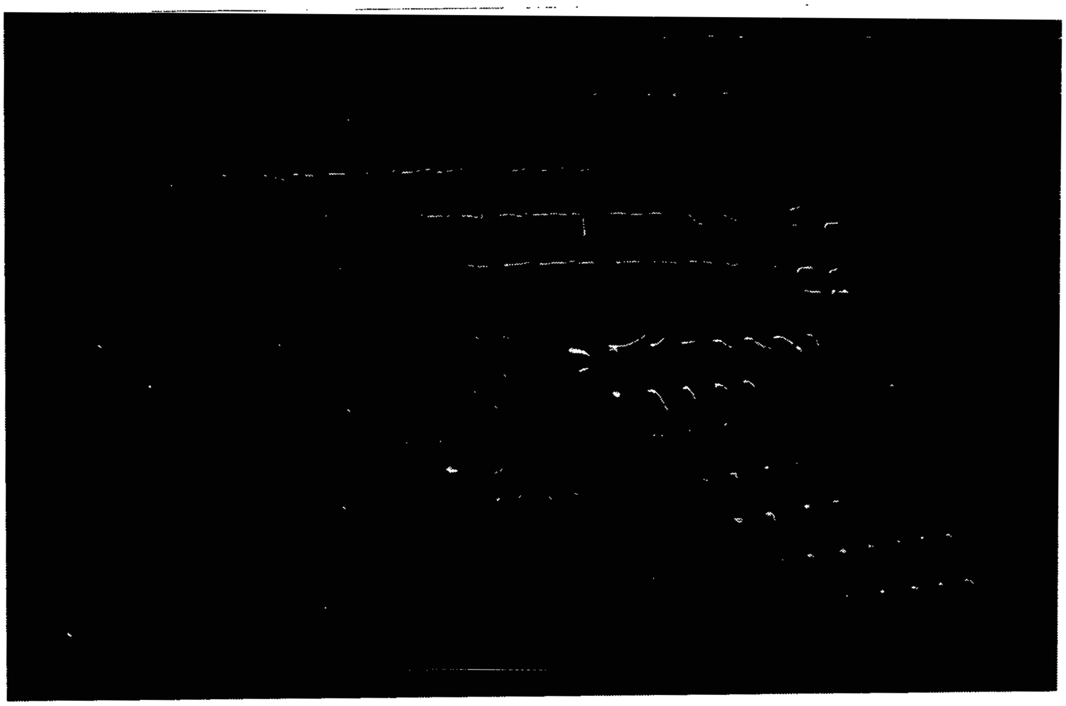

(c) $C_T = 0.9$.

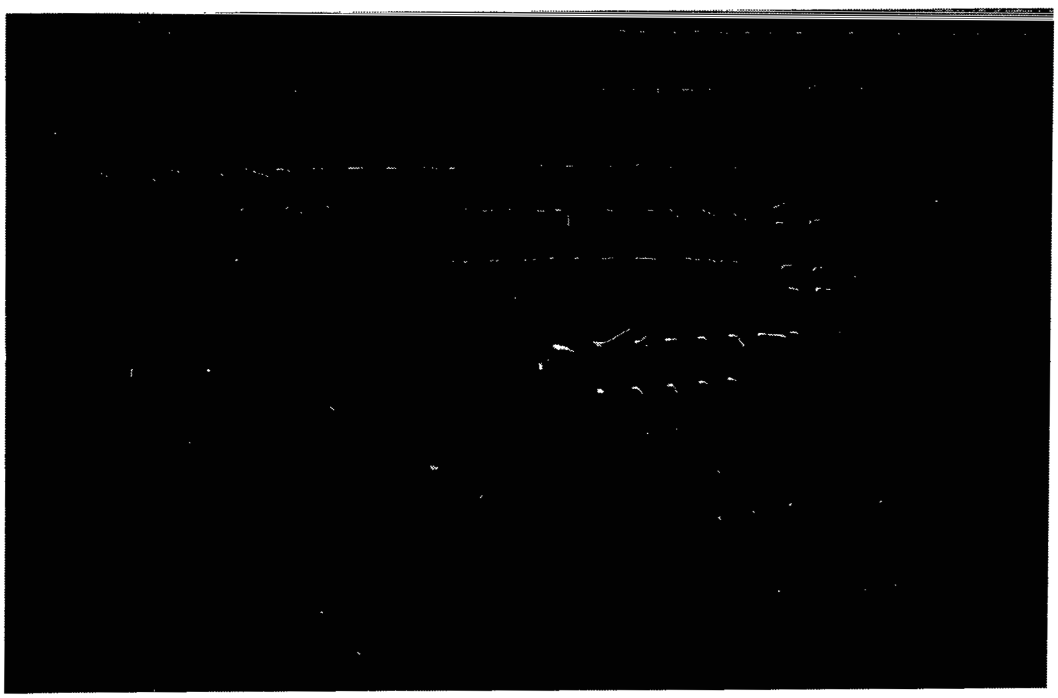

(d) $C_T = 1.5$.

L-83-122

Figure 30.- Concluded.

(a) $C_T = 0.$

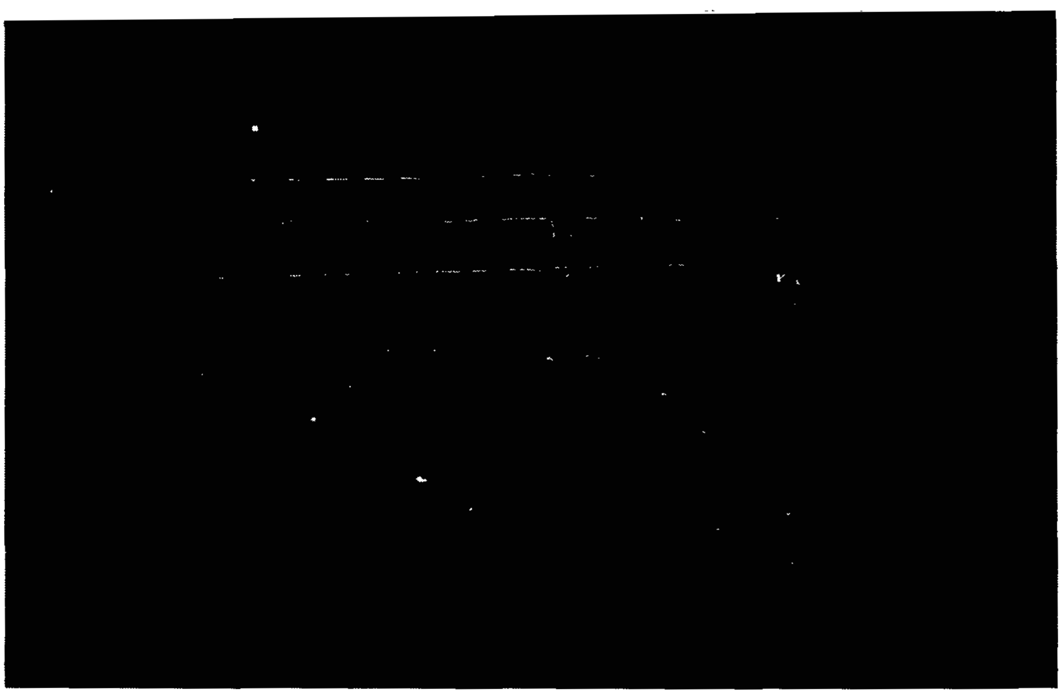

(b) $C_T = 0.2.$

L-83-123

Figure 31.- Minituft flow visualization of main and 40°-sweep spanwise-blowing nozzles for VEO-wing configuration with $\delta_f = 30°$ and $\alpha = 16°$.

(c) $C_T = 0.9$.

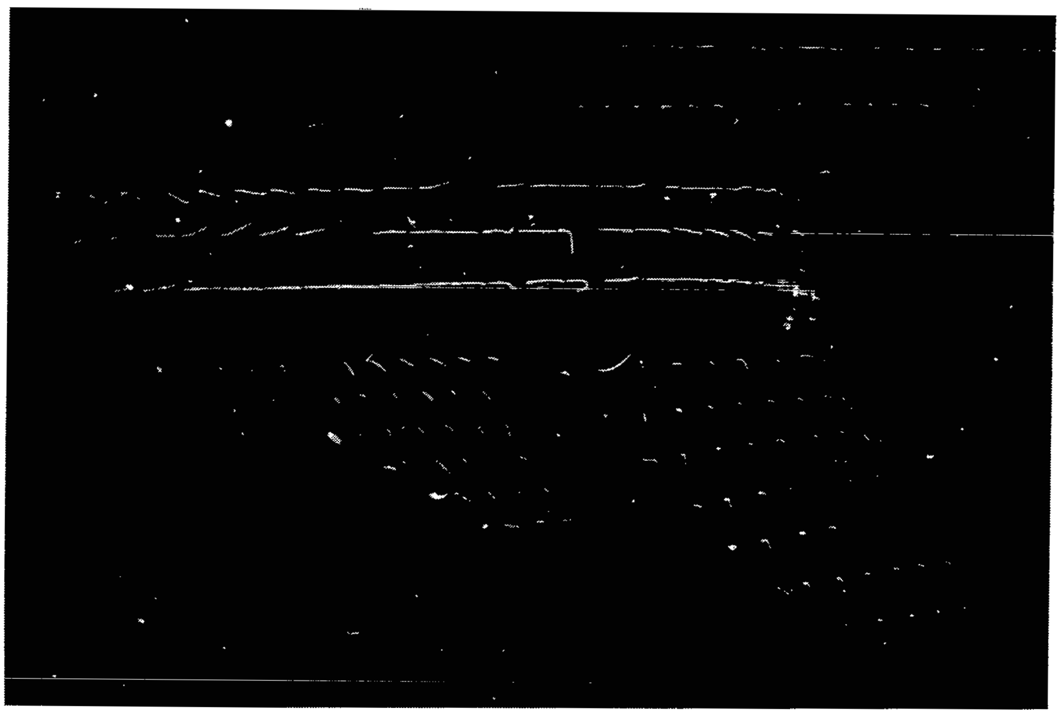

(d) $C_T = 1.5$.

L-83-124

Figure 31.- Concluded.

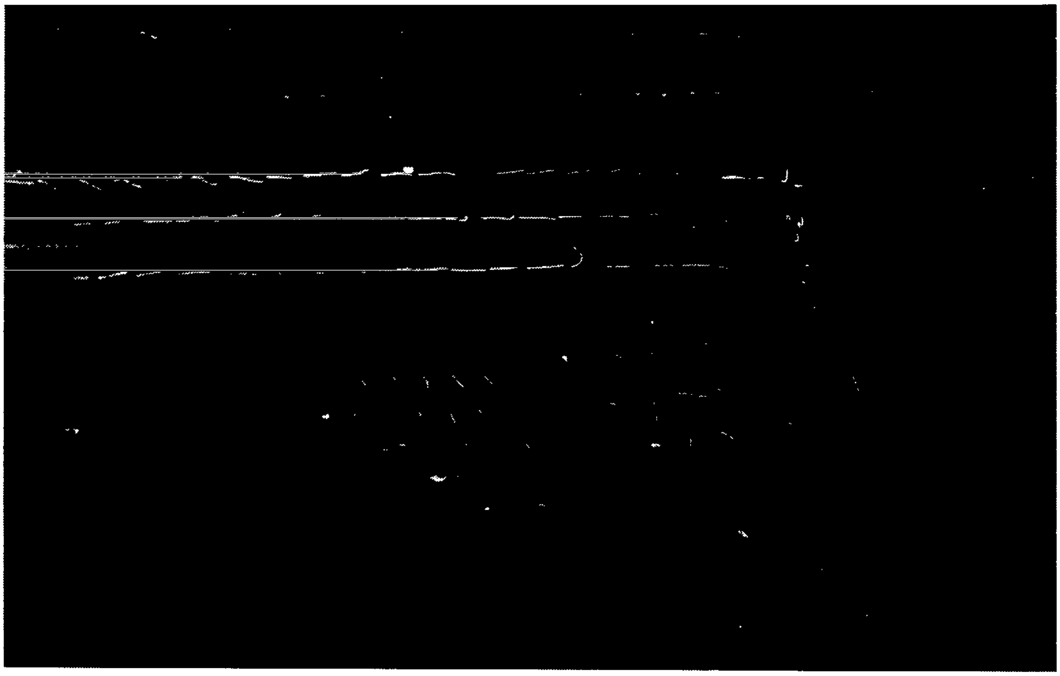

(a) $C_T = 0.$

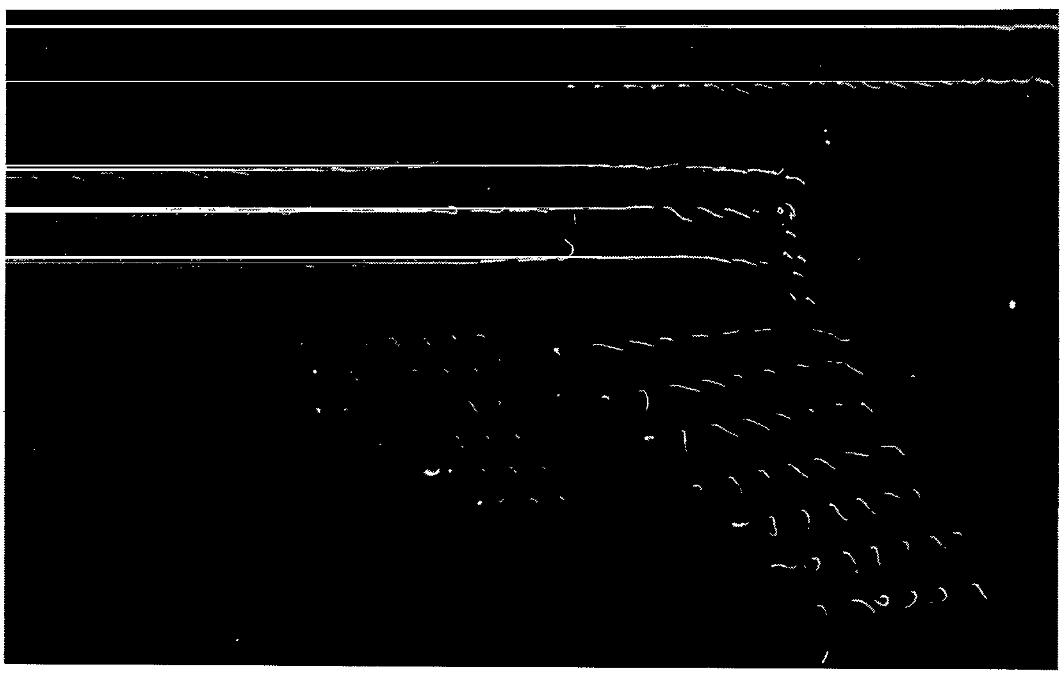

(b) $C_T = 0.2.$

L-83-125

Figure 32.- Minituft flow visualization of main and 60°-sweep spanwise-blowing nozzles for VEO-wing configuration with $\delta_f = 30°$ and $\alpha = 16°$.

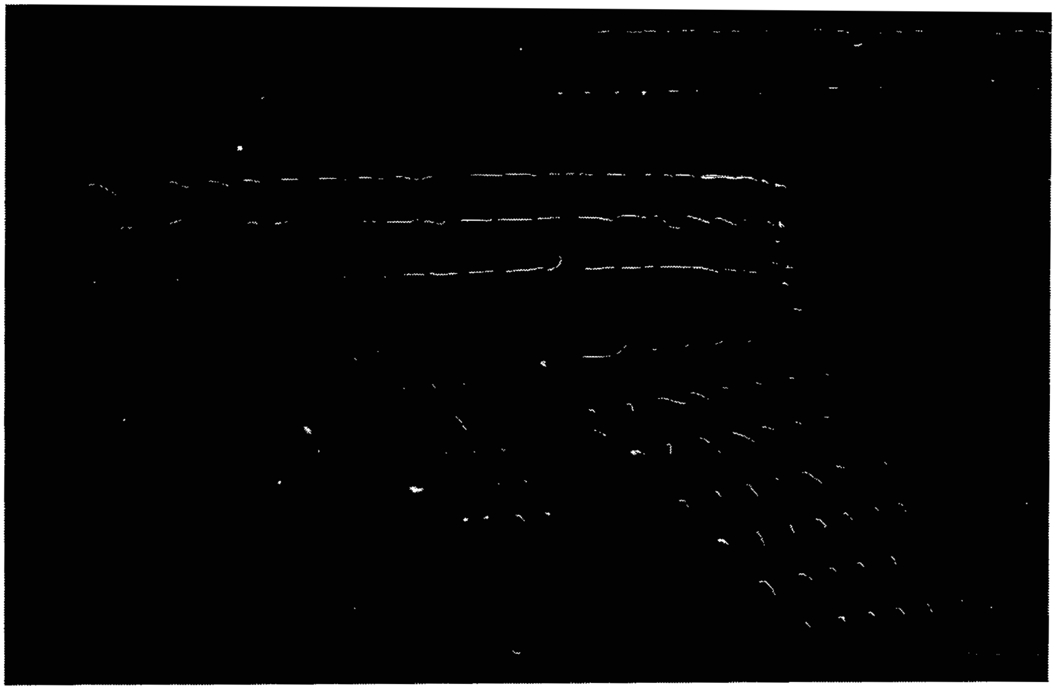

(c) $C_T = 0.9.$

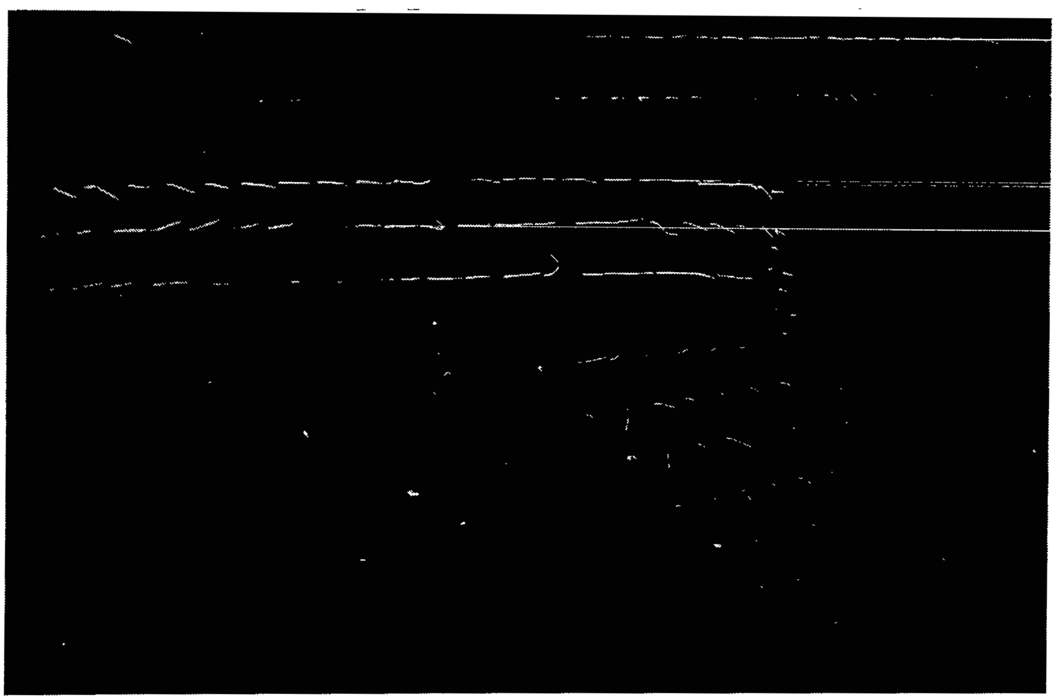

(d) $C_T = 1.5.$

L-83-126

Figure 32.- Concluded.

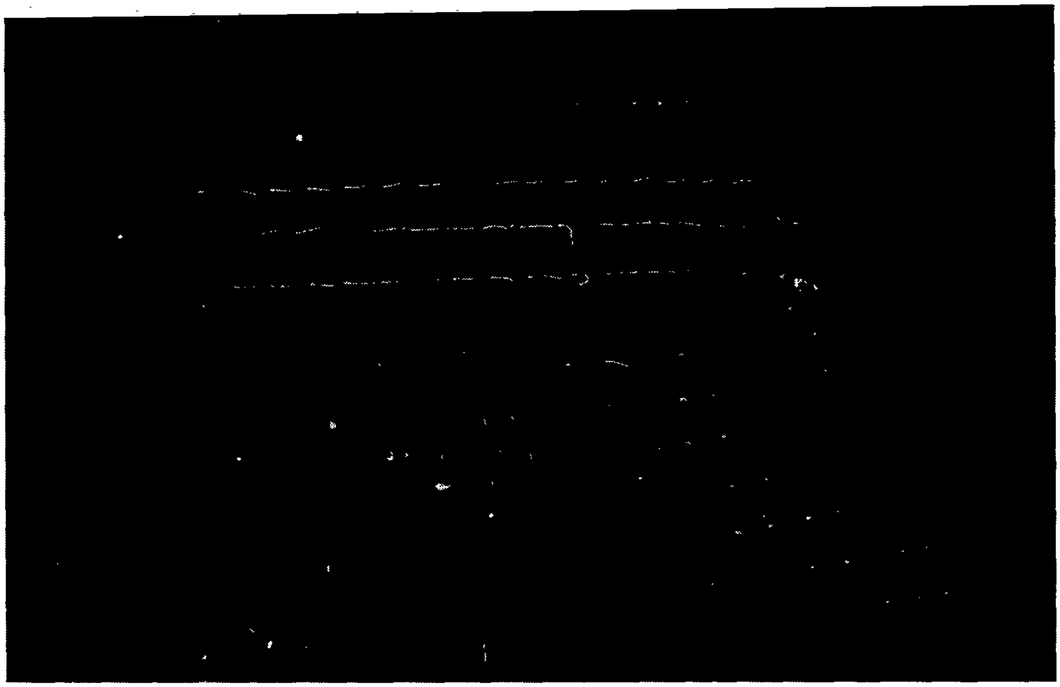

(a) $C_T = 0.$

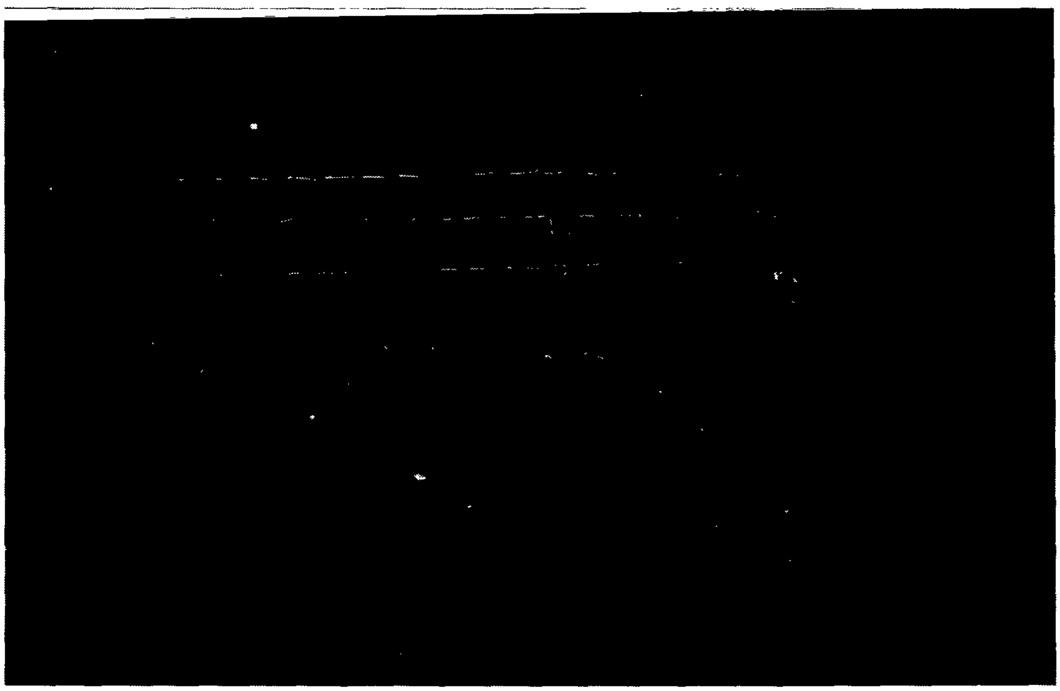

(b) $C_T = 0.2.$

L-83-123

Figure 31.- Minituft flow visualization of main and 40°-sweep spanwise-blowing nozzles for VEO-wing configuration with $\delta_f = 30°$ and $\alpha = 16°$.

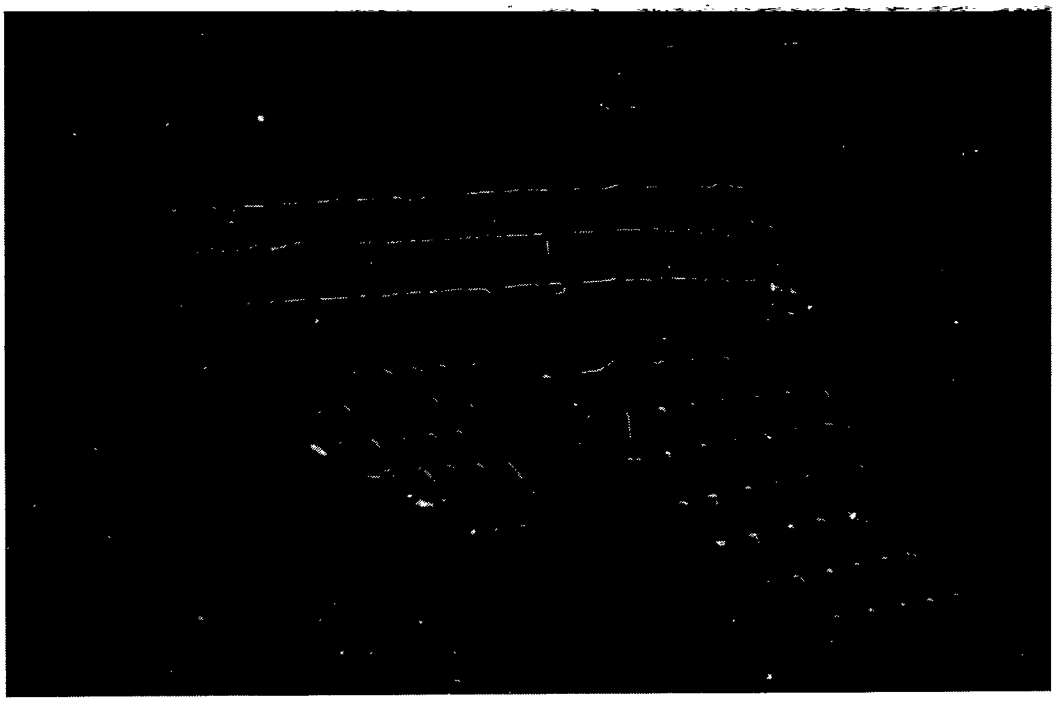

(c) $C_T = 0.9.$

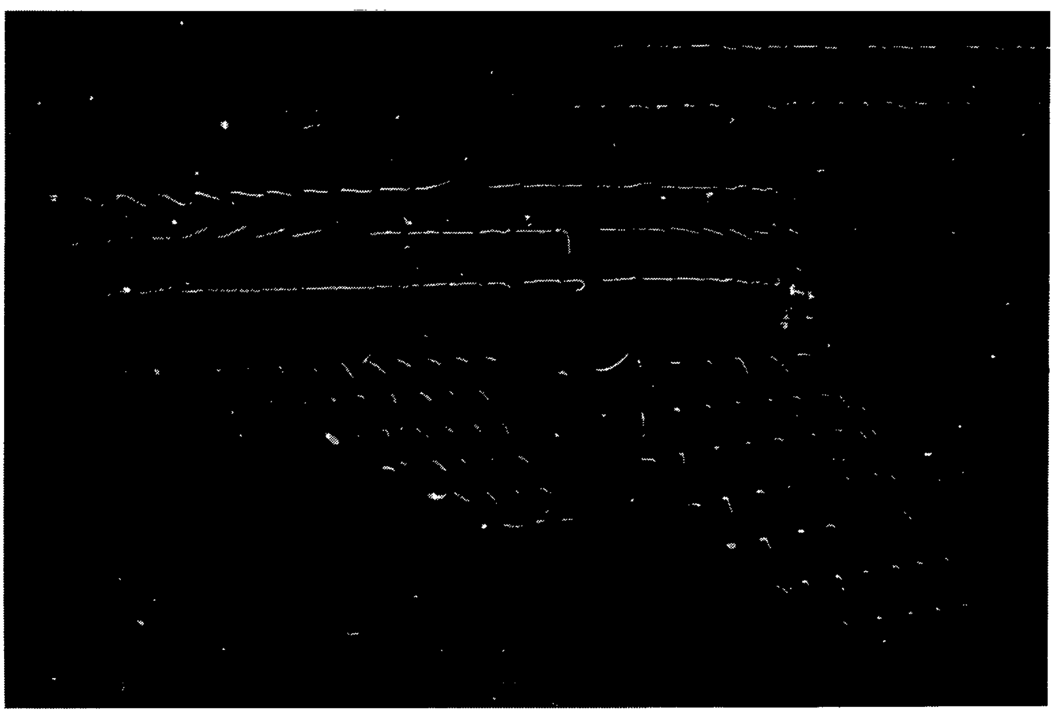

(d) $C_T = 1.5.$

L-83-124

Figure 31.- Concluded.

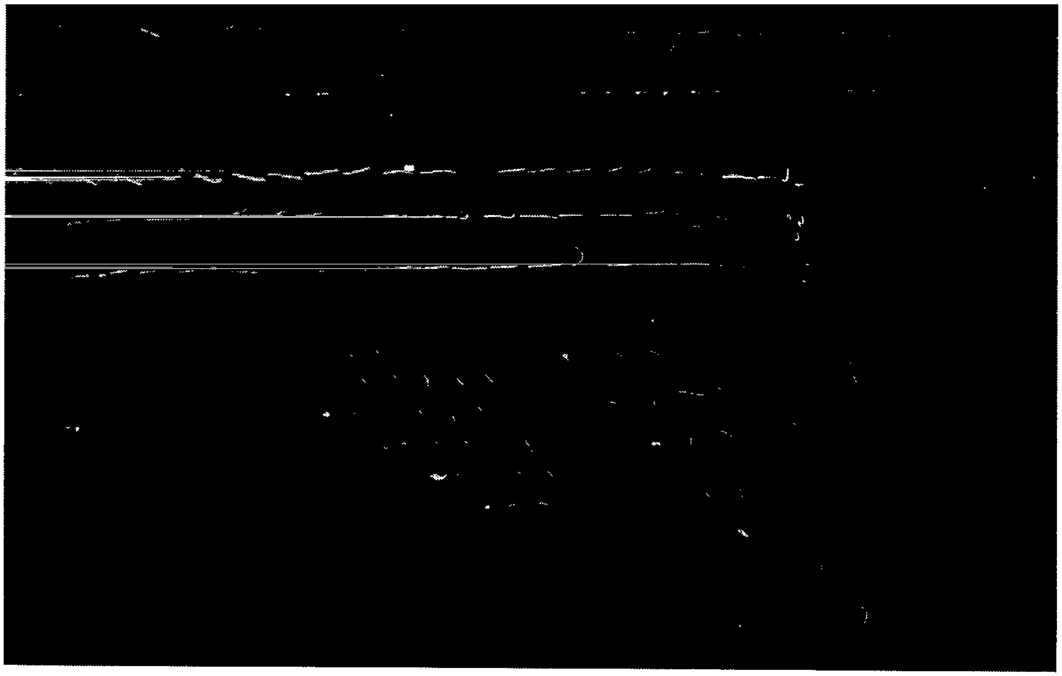

(a) $C_T = 0.$

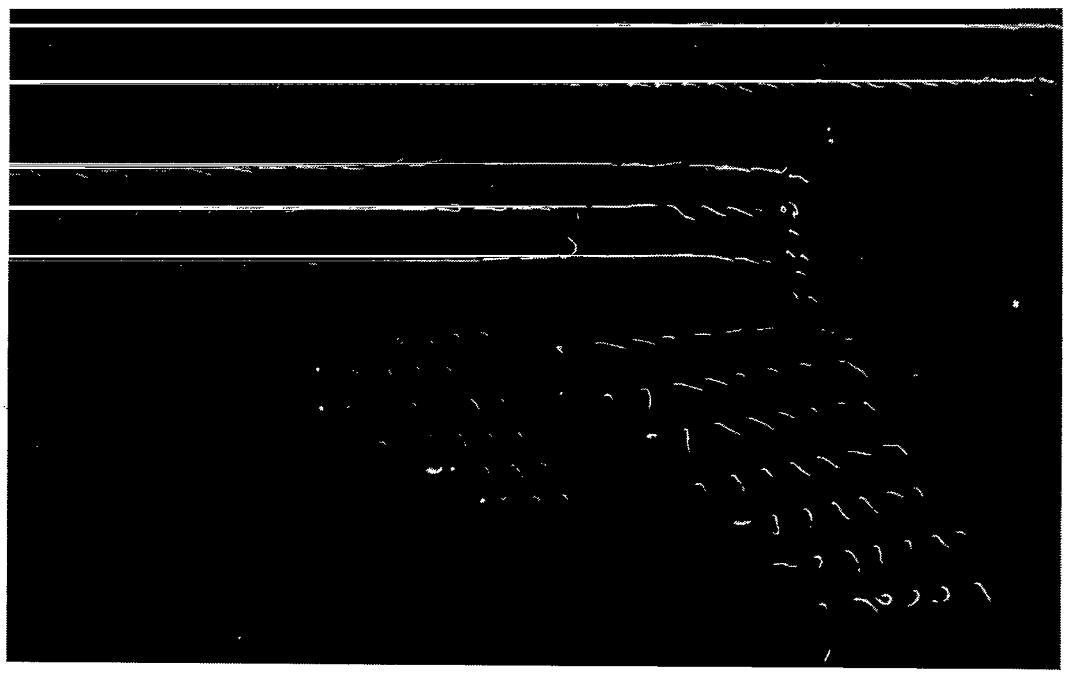

(b) $C_T = 0.2.$

L-83-125

Figure 32.- Minituft flow visualization of main and 60°-sweep spanwise-blowing nozzles for VEO-wing configuration with $\delta_f = 30°$ and $\alpha = 16°$.

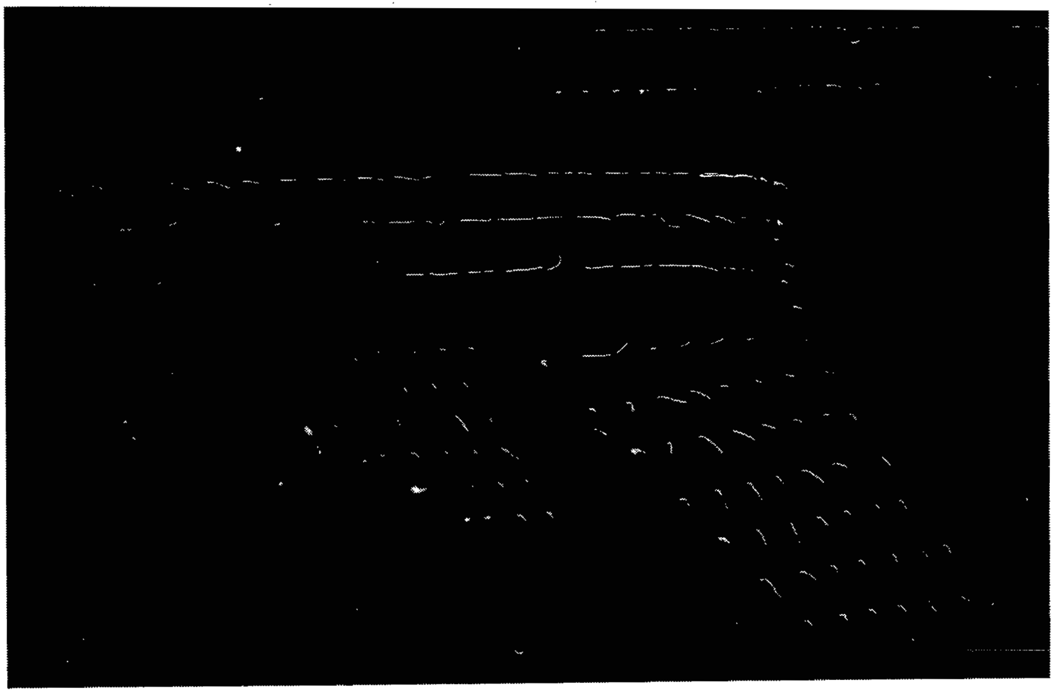

(c) $C_T = 0.9$.

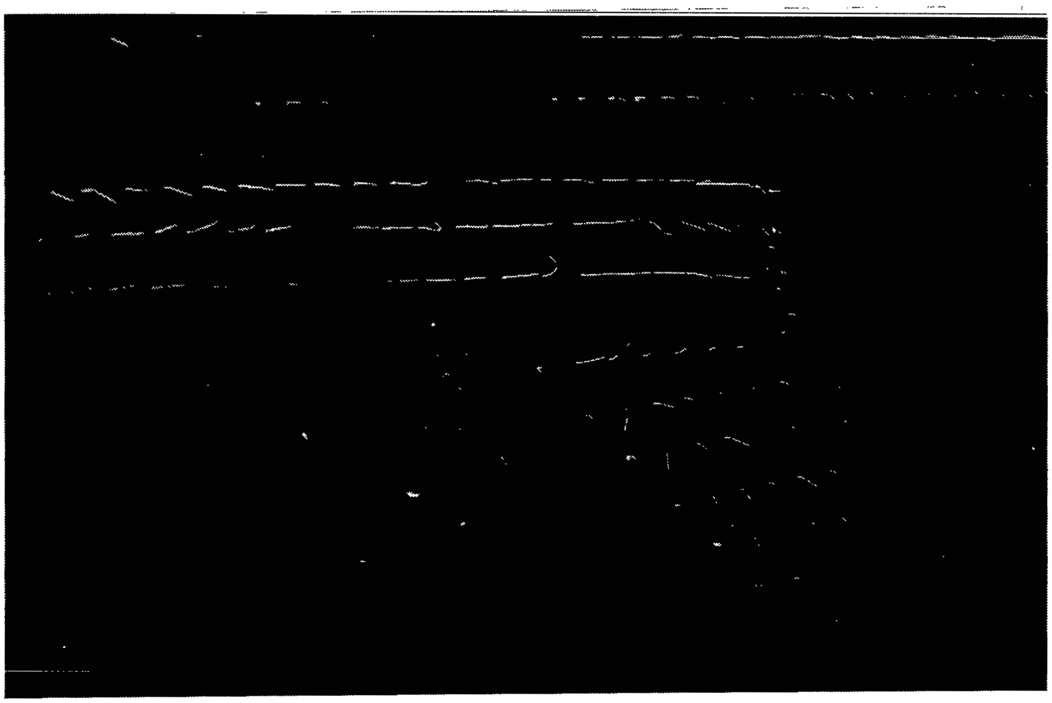

(d) $C_T = 1.5$.

L-83-126

Figure 32.- Concluded.

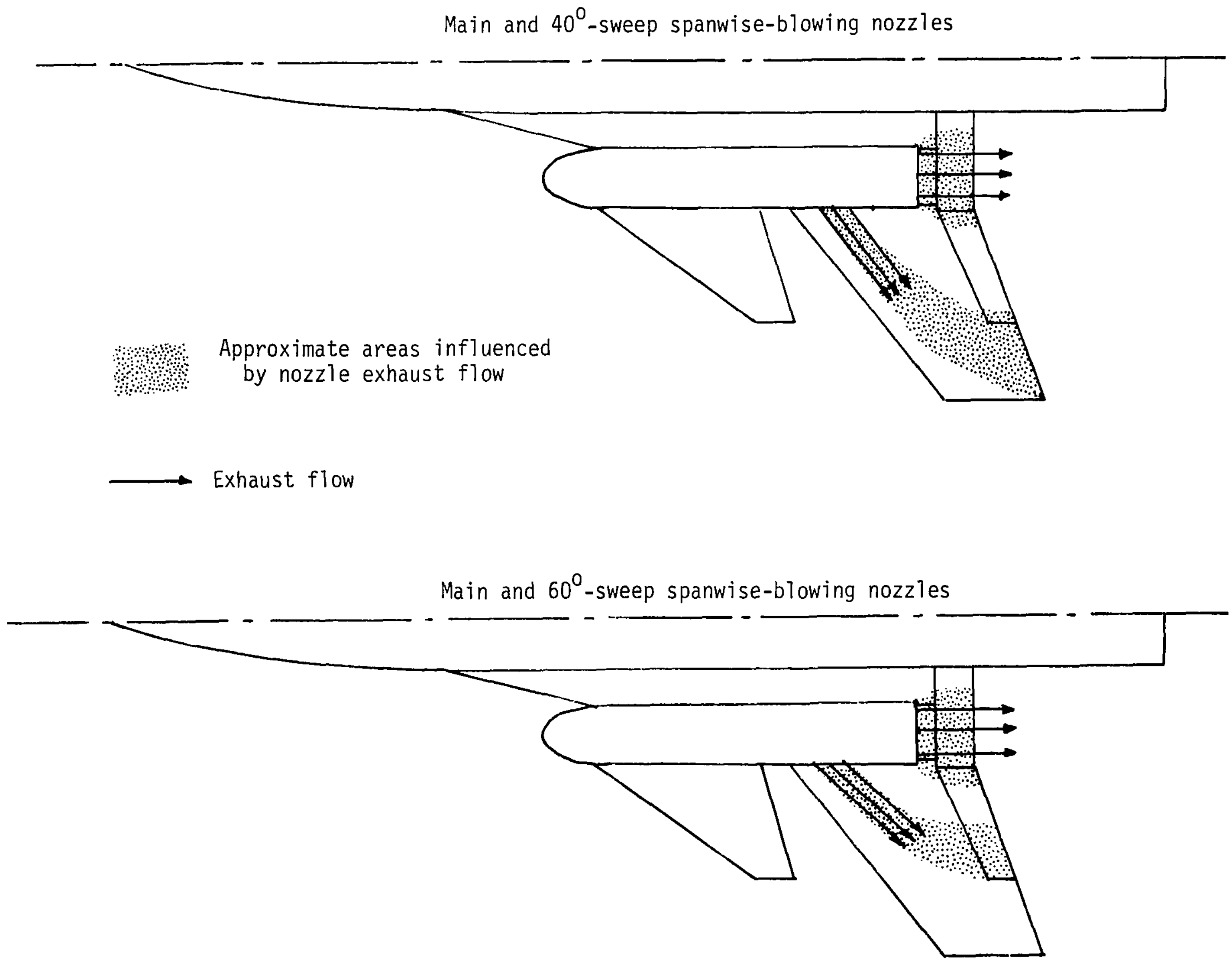

Figure 33.- Effects of nozzle exhaust on the VEO-wing configuration.

1. Report No.	2. Government Accession No.	3. Recipient's Catalog No.
NASA TP-2228		

4. Title and Subtitle	5. Report Date
THRUST-INDUCED EFFECTS ON SUBSONIC LONGITUDINAL AERODYNAMIC CHARACTERISTICS OF A VECTORED-ENGINE-OVER-WING CONFIGURATION	December 1983
	6. Performing Organization Code 505-43-23-04
7. Author(s) P. Frank Quinto and John W. Paulson, Jr.	8. Performing Organization Report No. L-15629
	10. Work Unit No.
9. Performing Organization Name and Address NASA Langley Research Center Hampton, VA 23665	11. Contract or Grant No.
	13. Type of Report and Period Covered Technical Paper
12. Sponsoring Agency Name and Address National Aeronautics and Space Administration Washington, DC 20546	14. Sponsoring Agency Code

15. Supplementary Notes

16. Abstract

An investigation was conducted in the Langley 4- by 7-Meter Tunnel of the thrust-induced effects on the longitudinal aerodynamic characteristics of a vectored-engine-over-wing fighter aircraft. The investigation was conducted at Mach numbers from 0.14 to 0.17 over an angle-of-attack range from -2° to 26°. The major model variables were the spanwise-blowing nozzle sweep angle and the main nozzle vector angle along with trailing-edge flap deflections. The overall thrust coefficient (main and spanwise nozzles) was varied from 0 (jet off) to 2.0. The results of the investigation indicate that the thrust-induced effects from the main nozzle alone were small and mainly due to boundary-layer control affecting a small area behind the nozzle. When the spanwise-blowing nozzles were included, the induced-effects were larger than the main nozzle alone and were due to both boundary-layer control and induced circulation lift. No leading-edge vortex effects were evident.

17. Key Words (Suggested by Author(s))	18. Distribution Statement
Thrust-induced effects Vectored engine over wing STOL fighter	Unclassified - Unlimited Subject Category 02

19. Security Classif. (of this report)	20. Security Classif. (of this page)	21. No. of Pages	22. Price
Unclassified	Unclassified	54	A04

For sale by the National Technical Information Service, Springfield, Virginia 22161

NASA-Langley, 1983

National Aeronautics and
Space Administration

Washington, D.C.
20546

Official Business
Penalty for Private Use, $300

THIRD-CLASS BULK RATE

Postage and Fees Paid
National Aeronautics and
Space Administration
NASA-451

U.S.MAIL

0 1 1J,A, 831215 S00903DS
DEPT OF THE AIR FORCE
AF WEAPONS LABORATORY
ATTN: TECHNICAL LIBRARY (SUL)
KIRTLAND AFB NM 87117

NASA

POSTMASTER: If Undeliverable (Section 158
Postal Manual) Do Not Return